The role of chromium content in aqueous passivation of a non-equiatomic Ni38Fe20CrxMn21-0.5xCo21-0.5x multi-principal element alloy (x = 22, 14, 10, 6 at%) in acidic chloride solution

Angela Y Gerard, Elizabeth J Kautz, Daniel K Schreiber, Junsoo Han, Stephen Mcdonnell, Kevin Ogle, Pin Lu, James E Saal, Gerald S Frankel, John R Scully

The Role of Chromium Content on Aqueous Passivation of Non-Equiatomic $Ni_{38}Fe_{20}Cr_xMn_{21-0.5x}Co_{21-0.5x}$ Multi-Principal Element Alloy (x = 22, 14, 10, 6 at. %) in Acidic Chloride Solution

Authors: Angela Y. Gerard[a,b], Elizabeth J. Kautz[c], Daniel K. Schreiber[c], Junsoo Han[a,b,d], Stephen McDonnell[b], Kevin Ogle[e], Pin Lu[g], James E. Saal[h], Gerald S. Frankel[f], John R. Scully[a,b]

Affiliations:

[a]*Center of Electrochemical Science and Engineering, University of Virginia, Charlottesville, VA 22904, USA*

[b]*Department of Materials Science and Engineering, University of Virginia, Charlottesville, VA 22904, USA*

[c]*Energy and Environment Directorate, Pacific Northwest National Laboratory, Richland, WA, 99352, USA*

[d]*Sorbonne Université, Laboratoire Interfaces et Systèmes Electrochimiques, LISE, F-75005 Paris, France*

[e]*Chimie ParisTech, PSL Université, CNRS, Institut de Recherche Chimie Paris (IRCP), F-75005 Paris, France*

[f]*Department of Materials Science and Engineering, Ohio State University, Columbus, OH, 43210, USA*

[g]*Questek Innovations LLC, Evanston Il, 60201, USA*

[h]*Citrine Informatics, Redwood City, CA, 94063*

Abstract

The effect of the Cr content on the corrosion behavior in a series of single-phase non-equiatomic $Ni_{38}Fe_{20}Cr_xMn_{21-0.5x}Co_{21-0.5x}$ ($6 < x < 22$ at. %) multi-principal element alloys (MPEAs) was investigated in acidified NaCl solutions. Comparisons were made with binary solid solution Co-Cr, Ni-Cr, and Fe-Cr alloys over a similar range of Cr contents. The corrosion behavior was evaluated using in-situ AC and DC electrochemical methods and ex-situ surface sensitive characterization techniques. Passivity and various levels of local corrosion resistance was obtained in the MPEA with 10 at. % Cr and above. The binary Ni-Cr alloys with 12 – 30 at. % Cr behaved similarly. The MPEA with 6 at. % Cr and binary alloys with 5, 6, or 10 at. % Cr were marginally passive or active and underwent localized corrosion during both linear sweep voltammetry and potentiostatic hold experiments. Passive films formed during potentiostatic hold experiments were characterized with X-ray photoelectron spectroscopy and atom probe tomography. Cr cation enrichment in the passive films was observed for all alloys and similar enrichment factors were obtained as a function of Cr content regardless of whether MPEA or binary alloy except for the Fe-Cr alloy. Moreover, passive current density was correlated with the Cr cation fraction in the passive film. The degree of Cr enrichment was attributed to a combination of thermodynamic and kinetic factors, such as selective chemical dissolution of alloying elements as well as limitation due to solute depletion at the metal oxide interface in alloys with a bulk Cr content ≤ 10 at. %.

1. Introduction

It is well known that Cr plays a critical role in corrosion resistant alloys toward corrosion resistance in a number of aqueous environments. For example, the effect of Cr on the passivity of a system has been extensively studied in binary (i.e., Fe-Cr, Ni-Cr, Co-Cr)[1-11] and ternary (i.e., Ni-Cr-Mo, Fe-Ni-Cr) [2, 11-19] alloy systems. In complex alloys, such as stainless steels, the alloy becomes more likely to passivate and exhibit a significant decrease in passive current density (i_{pass}) with increasing bulk Cr concentration.

Improved passivity with increasing Cr content has at times been described via a critical Cr concentration above which the alloy becomes effectively "fully passive" to a given environment. By extension, at bulk Cr concentrations above the critical Cr concentration, the alloy is expected to form a passive film at similarly low levels of critical potential and current density [5-10, 14, 18-20]. Conversely, below the critical Cr concentration, passive films formed on Fe-Cr or Ni-Cr alloys are generally described as more "Fe-like" or "Ni-like" with inferior corrosion resistances [5, 21]. For example, Asami et al. investigated the passive films formed on a series of Fe-xCr binary alloys ($10 < x < 80$ at. %) in deaerated 1 M Na_2SO_4 solution at a passivating potential of 500 mV versus saturated calomel electrode (SCE). The passive films were characterized by X-ray photoelectron spectroscopy (XPS) and showed a change in Cr passive film composition at bulk Cr concentrations greater than 12.5 at. %. It was concluded that at a low Cr concentration (i.e., 10 at. %) the passive film consisted mainly of Fe hydroxide species while at bulk Cr concentrations $\geq$ 12.5 at. %, the film consisted of Cr hydroxide species [5]. Different critical Cr concentrations, depending on the alloying elements, have been reported [6, 7, 22]. For Fe-Cr alloys, a critical Cr content of 13 at. % has been reported [7, 10, 23], and for Co-Cr alloys 9 at. % Cr critical content was documented [6]. Theoretical models have been

proposed to account for the origin of the critical Cr content such as graph [8, 9, 18, 22-25] and percolation theory [21, 26-28]. Commonly, these investigations report critical values in aqueous solutions that do not contain Cl^-, which has shown to influence an alloys passive behavior [29-31].

Fe-Mn and Ni-Mn binary alloys are reported to form relatively unprotective passive films in aqueous Cl^- solutions [11, 32-39]. Improved corrosion resistance of such systems could be achieved by adding Cr but these are inferior to alloys without Mn [40]. Zhu et al. investigated a series of Fe-Mn-xCr alloys ($1 < x < 7$ wt. %) [11]. These alloys showed lower corrosion current densities and increased corrosion potentials with increasing alloy Cr concentration in a 1 M Na_2SO_4 solution. The alloys also exhibited a less pronounced active-to-passive current density transition and broader passive potential regions with increasing Cr content during potentiodynamic polarization experiments [11]. They observed that the 7 wt. % Cr alloy exhibited lowest passive current density of 1×10^{-5} A cm^{-2}. In chloride-containing solution (3.5 wt. % NaCl), the Fe-Mn-xCr alloys did not show a clear passive potential domain, although the corrosion current densities decreased and corrosion potentials increased with bulk Cr content [11]. In the case of Ni-Cr-Mo alloy systems, lower passive current densities were observed for Ni-Cr-Mo alloys with bulk Cr $\geq$ 20 at. % compared to 16 at. % in NaCl + H_2SO_4 solution [14]. Vigorous testing has been conducted on binary and ternary alloy systems but information is lacking on the effects of Cr content on alloys containing five or more alloying elements.

Multi-principal element alloys (MPEAs) have unusual attributes in which provide the opportunity for unique combinations of properties that may make them interesting candidates for corrosion resistant alloys[41]**.** However, relatively little is known about the dependencies on the corrosion mechanism of MPEA passivity on Cr content compared to the binary and ternary

alloys. In particular, it has yet to be established how the MPEA alloy complexity may affect Cr enrichment in passive films and resulting passivity as a function of Cr content. Systematic studies of Cr content and details on the electrochemical passive response as a function of bulk and film Cr concentrations are lacking, although numerous reports on MPEAs show that Cr is beneficial to the corrosion resistance of the passive film [32, 42-50]. Chai et al. investigated the role of Cr-induced segregation on the corrosion behavior of an $FeCoNiCr_x$ (Cr_x = 0, 13.22, 24.23 wt. %) MPEA [46]. Potentiodynamic polarization and electrochemical impedance spectroscopy (EIS) were utilized to evaluate the corrosion properties and passivation mechanism in 0.5 M H_2SO_4 and 3.5 wt. % NaCl solutions at 25 °C. $FeCoNiCr_{13.22}$ MPEA showed enhanced corrosion resistance compared to the Cr_0 and $Cr_{24.23}$ MPEAs, as indicated by a more positive passivity breakdown potential, lower corrosion current density, and lower passive current density (i_{pass}), in each testing solution. The EIS characterization revealed that the $Cr_{13.22}$ addition stabilized the passive film because of higher oxide resistance compared to that of the Cr_0 MPEA. In the case of $Cr_{24.23}$ MPEA, the Cr addition resulted in a lower oxide resistance, indicating a less stable passive film formation. It was concluded that the high Cr concentration in the $Cr_{24.23}$ MPEA led to the development of new phases and a dendritic morphology with a heterogeneous Cr distribution. Cr partitioning in the $Cr_{24.23}$ MPEA resulted in a noncontinuous passive layer susceptible to localized corrosion [46].

Recent reports post detrimental corrosion behavior in MPEAs that contain more than 15% Mn in spite of a high Cr content. Yang et al. investigated the passivation behavior of CoFeNiMnCr MPEAs in H_2SO_4 solution [48]. Two sets of MPEAs were explored containing Mn where the Cr concentration was set to 20 and 25 at. %, CoFeNiMnCr and $(CoFeNiMn)_{75}Cr_{25}$, respectively. These were compared to MPEAs containing no Mn, $(CoFeNi)_{80}Cr_{20}$ and

$CoFeNiCr_{25}$. For both sets of MPEAs, a broad passive potential region was observed during potentiodynamic polarization experiments. The Cr-MPEAs with no Mn showed better corrosion resistance indicated by potentiodynamic polarization curves and EIS polarization resistance. The $(CoFeNi)_{80}Cr_{20}$ and $CoFeNiCr_{25}$ MPEAs showed slightly lower i_{pass} and significantly lower current densities in the region where an active to passive potential transition occurred than the Mn-containing alloys, i.e. ~10^{-4} A cm^{-2} for CoFeNiMnCr, vs. 10^{-5} A cm^{-2} for $(CoFeNi)_{80}Cr_{20}$ and 10^{-5} A cm^{-2} for $CoFeNiMn)_{75}Cr_{25}$ vs. 10^{-6} A cm^{-2} for $CoFeNiCr_{25}$ [48]. EIS analysis after a 1 hr stable open-circuit potential measurement showed that the polarization resistances of the $(CoFeNi)_{80}Cr_{20}$ MPEA and $CoFeNiCr_{25}$ MPEA were much higher than the Mn-containing MPEAs, suggesting the formation of a more protective passive film in the case of the Mn-free MPEAs. It was concluded that the addition of Mn decreased the general corrosion resistance of the MPEAs by forming a relatively unstable passive film compared to the Mn-free MPEAs [48]. Another Cr-containing MPEA study showed similar results but also lacked a detailed analysis regarding current densities as a function of Cr concentration in the bulk and passive film [51].

Understanding the beneficial role and limitations of Cr content in MPEA passivity, and potential synergistic or detrimental interactions with the diversity of other alloying elements requires a detailed analysis of passive films formed during aqueous oxidation on Cr-containing MPEAs. At the same time, comparisons with simpler systems such as binary alloys with similar bulk Cr concentrations are critical to identify more complex interactions. To explore these effects further, the corrosion protectiveness of the formed passive films must be studied for varying alloy Cr content. This requires a complex set of analytical datasets, including valence states present in the passive film, elemental composition, and cation distribution in conjunction with its electrochemical corrosion behavior. Complementary techniques, including XPS and atom probe

tomography (APT), are ideal in this context to provide quantitative analyses of nanoscale elemental segregation and partitioning, localized enrichment/depletion, and chemical states.

In this study, a series of non-equimolar, single phase, solid solution $Ni_{38}Fe_{20}Cr_xMn_{21-0.5x}Co_{21-0.5x}$ MPEAs previously reported [32, 35, 52-55], where x = 6 - 22 at. %, were compared to a series of high-purity Ni-Cr, Fe-Cr, and Co-Cr binary alloys. The goal of this investigation was to enhance the understanding of the role of Cr in the corrosion properties of transition metal MPEAs for the condition when the sum of the other elements in the MPEA is equivalent to the solvent concentration in binary alloys and bulk Ni and Fe content are kept constant in the MPEAs. Explored herein are (a) the enrichment and/or depletion of Cr throughout the passive film; (b) comparison of Cr-containing MPEAs to similar Cr-containing binary alloys at low, intermediate, and high Cr contents; (c) possible explanations for Cr enrichment or depletion expressed as cation fraction in the oxide/hydroxide film as well as the possible governing factors.

2. Experimental

The $Ni_{38}Fe_{20}Cr_xMn_{21-0.5x}Co_{21-0.5x}$ – at. % MPEAs were arc-melted, cast, and homogenized at 1100 °C for 96 hours using methods described previously [52]. Within this region, a single FCC phase solid solution is stable over a range of Cr concentrations, where x = 22, 14, 10, 6 at. %, compensated by variable Mn and Co concentrations. For simplicity, these MPEAs will be referred to as Cr22-, Cr14-, Cr10-, and Cr6-MPEA, respectively. Fe-xCr (x = 30, 20, 10, 5 at. %) binary alloys were produced from pure elemental Fe and Cr (> 99 % purity). The Fe was placed on the bottom of the crucible and the Cr was placed on top because of its higher melting point. The precursor materials were vacuum arc-melted in a water-cooled copper crucible under an Ar atmosphere of 0.5 atm pressure. The buttons were flipped and re-melted under similar conditions for a minimum of five times to ensure homogeneity. The ~10 g buttons were cut by electrical

discharge machining into 2 mm slices. The sliced Fe-30Cr and Fe-20Cr samples were further homogenized at 1100 °C for 2 hr to obtain a BCC solid solution phase. Similarly, the Fe-10Cr and Fe-5Cr samples were homogenized at 700 °C for 24 hr to obtain a BCC solid solution phase. The Co-xCr alloys (x = 30, 20, 10, 5 at. %) were fabricated from pure elemental Co and Cr (> 99 % trace metal basis) with a multistep vacuum arc-melting process similar to the Fe-Cr alloys. The Co-xCr alloy slices were homogenized at 1100 °C for 24 hr to obtain an FCC solid solution phase. A series of Ni-xCr binary alloys (x = 30, 20, 10, 5 at. % Cr) were cast from ultra-high purity Ni base material and ultra-high purity Cr. Samples were hot forged at 900 °C followed by a solution anneal at 950 °C for 1 hr and water quenched [56]. For passive film characterization, separate Ni-Cr alloys were used. These alloys were solid solution Ni-24Cr and Ni-12Cr (at. %) binary alloys that were arc-melted, cast, rolled, solutionized at 1100 °C, and recrystallized, resulting in a homogenous single-phase FCC alloy [57, 58]. All tested materials and corresponding compositions are listed in **Table 1**.

For electrochemical testing, samples were mechanically ground to 1200 grit using SiC, degreased with acetone, rinsed with deionized water, and dried with $N_{2(g)}$. For potentiostatic passivation and characterization experiments, samples were mechanically ground to 1200 grit using SiC, polished with 0.25 µm diamond suspension, and then polished with colloidal silica with a final finish of 0.06 µm. Samples were degreased after polishing by sonicating in acetone, 1:1 acetone and isopropanol, isopropanol, and deionized water, each for 1 min, and dried with $N_{2(g)}$.

Electrochemical tests were conducted in $N_{2(g)}$ – deaerated 0.1 M and 1 mM NaCl, with the final pH adjusted to 4 using 0.1 M HCl. The 1 mM NaCl electrolyte was utilized for electrochemical passivation experiments, in order to evaluate the passivation of low Cr-alloys for

comparison to high Cr-alloys within a slightly acidified Cl^- environment. Experiments were performed with a Gamry Instruments Reference 600+™ potentiostat. A standard three-electrode cell was utilized with a Pt mesh counter electrode, a SCE reference electrode and an MPEA or binary alloy sample as the working electrode. Samples were pressed against a rubber O-ring to expose an area of 0.1 cm^2. All potentials are reported against SCE.

Linear sweep voltammetry (LSV) experiments (potentiodynamic) were conducted over a range of applied potentials (-1.3 V_{SCE} to 0.8 V_{SCE}) with a scan rate of 0.5 mV s^{-1}. Prior to polarization, samples underwent an initial potentiostatic hold of -1.3 V_{SCE} for 600 s to minimize the effect of the air-formed oxide after polishing procedure. During LSV, the imaginary impedance component (-Z") was monitored at an applied AC voltage of 20 mV_{RMS} at f =1 Hz.

Electrochemical passivation was investigated within the passive potential region by potentiostatic passivation, where the passive potential was determined from LSV. Potentiostatic passivation was conducted using the following procedure: (1) cathodic treatment to minimize the effect of the air-formed oxide at -1.3 V_{SCE} for 600 s, (2) step potential hold at 0.0 V_{SCE} within the passive potential region for 10 ks, followed by (3) an EIS measurement from 100 kHz to 1 mHz at the same potential as (2). During the potentiostatic hold experiment, passive film growth was monitored as a function of time using a single-frequency EIS method (SF-EIS) at 1 Hz and an AC potential magnitude of 20 mV_{rms} [54, 57, 59]. All EIS data were analyzed with an equivalent circuit model initially established for alloy C-22 and adapted for MPEAs [13, 54, 59, 60]. Approximate oxide thickness (ℓ_{ox}) as a function of time was calculated based on the relationship between the equivalent circuit model, constant phase element exponential, and -Z", equation and methodology shown elsewhere [54, 57, 59]. The associated fitting parameters for all alloys and

the assumed oxide dielectric constants are tabulated in **Supplemental Tables S1 and S2**, respectively.

The charge efficiency (q_{ox}/q_{total}) of each passive film formed at 0.0 V_{SCE} was calculated from the total electrochemistry charge (q_{total}) and oxide charge (q_{ox}) densities over 10 ks or until a steady state passive current density was obtained. Oxide charge densities for the exact same conditions was calculated utilizing the relationship shown in Eq. 1;

$$q_{ox} = \frac{\ell_{ox} n F \rho}{M} \quad (1)$$

Where ℓ_{ox} is the EIS derived oxide thickness, , M is the oxide molar mass, n is the number of electrons transferred to produce the oxide from its elements, ρ is the oxide density of assumed oxides, and F is the Faraday constant (96485 C mol^{-1}). Hydroxides were considered as well as oxides. For charge calculations, weighted averages for M, ρ, and n were used for each alloy and oxides based on XPS cation fractions, as shown in supplemental information **Tables S2 and S3**.

XPS spectra were acquired using Al Kα X-rays (binding energy: 1468.7 eV) with a take-off angle of 45° at a pass energy of 26 eV with a spot size of 100 µm and an analysis depth of < 10 nm in a PHI VersaProbe III™ system. Cation fraction within the passive film and elemental composition just below the metal/film interface (relative to all cations or elements detected) were determined by spectral deconvolution of individual core-level spectra with KOLXPD™ analysis software. Spectral deconvolution was implemented with Voigt functions for oxides, asymmetric Doniach Sunjic-like features for metals, and a Shirley background subtraction [61, 62]. For each alloying element, the 2p core feature was deconvoluted utilizing reported parameters for multiplet splitting of reference stoichiometric compounds [63]. Due to Ni Auger overlap with Mn $2p_{3/2}$, Co $2p_{3/2}$, and Fe $2p_{2/3}$ spectra, the $2p_{1/2}$ feature was utilized for XPS spectral

deconvolution. A peak intensity limit of less than or equal to the intensity of noise was considered for Co and Mn $2p_{1/2}$ spectra, in order to establish an upper limit to the Mn(II) and Co(II) fractions present within the passive film. A more detailed description of XPS spectral deconvolution has been provided previously [32, 54, 59].

APT was utilized to track elements and their distribution throughout the passive films and across the metal/film interface after the above electrochemical passivation procedure for the Cr22-, Cr10-MPEA, Fe-20Cr, and Co-20Cr in order to explore similar Cr levels and one low Cr level. Passive films formed at 0.0 V_{SCE} were coated with ≈ 20 nm Cr and ≈ 50 nm Ni using an ion beam sputtering system prior to APT sample preparation. This Ni/Cr bilayer was used as a marker for targeting the coating/passive film/alloy interfaces in the final APT needle apex. APT sample preparation was performed using an FEI Helios™ dual beam focused ion beam-scanning electron microscope (FIB-SEM) [64]. APT needles were prepared by depositing a Pt protective layer and extracting a cantilever from the sample with the base alloy/passive film and Ni/Cr coating. Samples were prepared so that the Ni/Cr capping layer/passive film/base alloy interfaces were perpendicular to the analysis direction.

A CAMECA local electrode atom probe (LEAP) 4000X HR APT system equipped with a 355 nm wavelength UV laser was used for APT data collection with the following user-selected parameters: 60 pJ/pulse laser energy, 125 kHz pulse repetition rate, 40 K specimen base temperature, and 0.003 detected ions/pulse detection rate. Data were reconstructed and analyzed using the Interactive Visualization and Analysis Software (IVAS), version 3.8.8 by CAMECA. Mass spectrum peak ranging is defined in supplemental **Figures S1-S3**. Elemental composition profiles were determined using the proximity histogram method across O isoconcentration surfaces (located at the approximate base alloy/passive film interface, which varied in at. % for

each alloy), with a bin width of 0.2 nm. The extracted concentration profiles were normalized to consider only alloy principal elements (i.e., excluding O or other trace species) to enable more direct interrogation of enrichment or depletion relative to the base alloy composition. Definitions of base alloy (metal)/passive film, and passive film/Cr cap interfaces are given in supplemental **Table S4**.

A surface enrichment-depletion calculation approach, developed by Castle and Asami [65], was utilized to calculate a cation/elemental enrichment or depletion term for chromium, f_{Cr}, within passive films formed during electrochemical passivation at 0.0 V_{SCE}. Cr Enrichment and depletion terms were determined from all cation fractions within the passive film ($f_{Cr,ox}$) from XPS as well as separately for the metallic concentration at the metal/film interface, hereafter referred to as the altered zone ($f_{Cr,az}$), determined from XPS and APT. The altered zone region within APT concentration profile was determined based on Ni and Cr concentrations just below the metal/film interface correlated with the oxygen isoconcentration surface (defined in supplemental information) and in conjugation with XPS elemental Ni and Cr concentrations (i.e. enriched metallic Ni and depleted metallic Cr). APT cation fractions for the altered zone and passive film were determined from taking the average atom concentration of each element within each region. By utilizing the relationship between passive film and altered zone f_{Cr} and bulk alloy concentration, the expected Cr concentration within the passive film and altered zone were predicted over a range of relevant bulk Cr concentrations [54, 65]. This was performed within the range of Cr solid solution contents indicated by CALPHAD for the Cr-MPEA alloy [52]. A key initial assumption was that the enrichment term is independent of bulk alloy Cr content. A more detailed enrichment methodology has been previous provided with equations in our prior work [54].

A hypothetical Cr depletion zone depth or size was calculated for a range of hypothetical charge efficiencies utilizing mass balance between bulk Cr concentration in the alloy necessary to supply the XPS-based Cr cation fraction reported for the passive film given its Cr content. An efficiency less than 100% means that a fraction of the Cr oxidized as Cr(III) was lost to the solution and does not contribute to the passive film thickness nor its composition. The following assumptions are considered: (a) the sum of Cr(III) in the oxide and dissolve must equal the mass balance removed from the metal altered zone, (b) the Cr concentration is zero (depleted at the oxide/metal interface) and depleted some alloy depth or "zone" required to achieve mass balance, (c) the oxide metal interface does not move or that vacancies injected as a result of metal dissolution are annihilated [66] and (d) Cr solid state diffusion through the altered zone is assumed to be equivalent in all alloys for the sake of this initial calculation.

3. Results

3.1. Electrochemical passivation behavior of Cr-MPEAs

LSV curves of the Cr-MPEAs and Cr binary alloys in deaerated 1 mM NaCl + HCl electrolyte and 0.1 M NaCl + HCl electrolyte at pH 4 solutions are shown in **Figs. 1** and **2**, respectively. The focus here is the electrochemical passivation and any active-passive transition observed during the upward potential scan. In each testing solution, the passive behavior (i.e., broader passive potential region, lower passive current densities, and higher breakdown potentials) was improved with increasing bulk Cr concentration for all materials.

The Cr-MPEAs showed passive potential regions at all Cr concentrations as indicated by a potential range greater than approximately 100 mV and current density below 10^{-4} A cm^{-2} in each solution (**Figs. 1** and **2**). In the case of the Fe-10Cr and Fe-5Cr binary alloys, active corrosion was exhibited with no evidence of passivity in each solution (**Figs. 1c and 2c**) as indicated by

large increases in anodic current density with applied potential, according to the criteria above. It should be noted, the Co-10Cr and -5Cr showed a small potential-passive region width of ~200 mV in 0.1 M NaCl prior to crevice corrosion (**Fig. 2d**). Ni-10Cr and Ni-5Cr also showed active corrosion in 0.1 M NaCl as shown in **Fig. 2b,** but they showed clearly defined passive potential domain in 1 mM NaCl solution as shown in **Fig. 1b**. In 1 mM NaCl solution, the Cr-MPEAs exhibited current spikes throughout their passive potential region, suggesting metastable pitting events (**Fig. 1a**). Zero current potentials were observed for Ni-30Cr in 1 mM NaCl and for Cr14-MPEA and Ni-24Cr in 0.1 M NaCl. The zero current potentials are an outcome from similarities between the passive current density and the limiting current for oxygen reduction caused by the presence of residual $O_{2(g)}$. It should be noted that pitting has been evaluated elsewhere on these MPEAs in Cl^- containing solutions and is not the focus of this work [53].

The Cr-MPEAs and Ni-Cr binary alloys showed passive current densities ranging from 10^{-6} to 10^{-5} A cm^{-2} during upward LSV in 1 mM NaCl solution, shown in **Fig. 1a**. In the case of the Fe-Cr binary alloys (**Fig. 1c**), Fe-30Cr and Fe-20Cr showed lower passive current densities (~1 x 10^{-6} A cm^{-2}) compared to the Cr-MPEAs**.** The Co-30Cr binary alloy (**Fig. 1d**) had a lower i_{pass} (~2 x 10^{-6} A cm^{-2}) compared to the Cr14, Cr10, Cr6-MPEAs and other low Cr content Co-Cr binary alloys. The binary Co-20Cr (**Fig. 1d**) alloy exhibited a low i_{pass} at more negative passive potentials, but at higher potentials its i_{pass} was slightly higher than that of the Cr22-MPEA. In 0.1 M NaCl solution, Cr22-MPEA exhibited a slightly lower i_{pass} compared to Ni-30Cr (**Figs. 2a and 2b**) and similar i_{pass} magnitudes (~10^{-6} A cm^{-2}) as Fe-30Cr and Co-30Cr (**Figs. 2c** and **2d**). The Cr14 and Cr10-MPEAs exhibited i_{pass} values similar to those of the Ni-20Cr, Fe-20Cr, and Co-20Cr binary alloys (**Fig. 2**).

The potential dependence of the imaginary impedance component (-Z'') at f = 1 Hz for Cr22-MPEA versus Ni-24Cr, and Cr6-MPEA versus Ni-5Cr is shown in **Figs. 3a and 3b**, respectively. At f = 1 Hz, -Z" scales linearly with oxide thickness given a fixed constant phase element exponential (α_f), shown in **Supplemental Table S1** [2]. The negative of the imaginary component of impedance, -Z", is small but increasing below and near the corrosion potential signaling passive film formation. Increases continue for all high Cr content alloys during upward linear voltage sweeps within the passive region (0.0 V_{SCE} < E < 0.4 V_{SCE}), The Cr22-MPEA indicated the highest -Z" values (**Fig. 3a**) in this potential region. In the case of the low Cr content alloys, the Cr6-MPEA and Ni-5Cr (**Fig. 3b**) also displayed an increase in -Z" at potentials from -1.0 V_{SCE} to -0.2 V_{SCE}. The Ni-5Cr binary alloy had a larger magnitude of -Z" compared to the 6Cr-MPEA at potentials greater than 0.0 V_{SCE}. At potentials above 0.31 and 0.37 V_{SCE}, -Z" begins to decrease for the Ni-24Cr and Cr22-MPEA (**Fig. 3a**), respectively, correlating with passive film breakdown. At potentials above 0.13 V_{SCE} for the Cr6-MPEA and 0.40 V_{SCE} for Ni-5Cr, -Z" also displayed a sudden decrease (**Fig. 3b**). The peaks in -Z" are suggestive of formation of specific oxides given the specific oxide formation potentials shown in **Supplemental Fig. S4**. However, there is not a direct correlation owing to kinetic factors such as the need for overpotentials.

The current densities in the passive potential domain at 0.0 V_{SCE} collected from LSV experiments for each alloy are summarized in **Fig. 4**. For each alloy class, the current density decreases with increasing Cr content in each testing solution. There is a large decrease in current density in 0.1 M NaCl between 10 and 20 % Cr for all alloys except Fe-Cr but exact threshold values cannot be determined. In 1 mM NaCl, all of the Cr-MPEAs and some binary alloys (Ni-Cr alloys at 10 and 5 at. % Cr, and all Co-Cr alloys) display similar current density (~10^{-4} A cm^{-2}),

as shown in **Fig. 4a**. The Fe-Cr binary alloys at 10 and 5 at. % Cr exhibited high current density values at 0.0 V_{SCE} (10^{-4} and 10^{-3} A cm^{-2}) compared to all alloys in both 1 mM and 0.1 M NaCl, respectively. In 0.1 M NaCl the Cr22, Cr14, Cr10, and Cr6-MPEAs had lower current densities at 0.0 V_{SCE} than all the binary alloys, as shown in **Fig. 4b**. A noteworthy observation is that the Cr10-MPEA exhibited much lower current density (10^{-4} A cm^{-2}) than any of 10Cr binary alloys, suggestive of superior protection.

3.2. Aqueous oxidation at an applied passive potential of 0.0 V_{SCE}

Passive current density decays during a potentiostatic hold at 0.0 V_{SCE} were utilized to characterize electrochemical passivation behavior. Current decays in 1 mM NaCl at 0.0 V_{SCE} for select alloys are shown in **Figs. 5** and **6**. Large decreases in the passive current density were observed for Cr22-, Cr14, Cr10-MPEAs, as well as Ni-24Cr, Ni-12Cr, Ni-10Cr, Fe-20Cr, Co-30Cr, and Co-20Cr during 10 ks potentiostatic hold (**Fig. 5).** The current density-time behavior was characterized by an initial plateau for ~ 10^2 seconds followed by a t^{-n} time dependency with n near 1. Metastable breakdown events were observed for most alloys as indicated by transient current density signal spikes, and more frequently for the Cr-MPEAs **(Fig. 5)**. Similar current density profiles were observed initially for Cr6-MPEA and Co-10Cr binary alloy at 0.0 V_{SCE} in **Fig. 6**. The current densities of the Cr6-MPEA and Co-10Cr binary alloy initially decrease indicating passivation, then sharply increase at longer times, t > 700 s and 2800 s, respectively. This increase in current density at 0.0 V_{SCE} signals passive film breakdown leading to localized corrosion, which was confirmed by the observation of crevice corrosion after the 10 ks of potential hold. Similar inferior passivation results are observed for Fe-Cr and Co-Cr binary alloys containing 5 and 10 at. % Cr, which indicates relatively inferior breakdown protection attributed to passive films formed on these alloys. In contrast, the Cr10-MPEA and Ni-10Cr

alloy showed clear evidence of sustained passivation indicated a continually decaying passive current density when held at the passive potential of 0.0 V_{SCE} as observed in **Fig. 5**.

Potentiostatic EIS was conducted at the end of the 10 ks hold at 0.0 V_{SCE} to monitor the impedance behavior of the film as well as to obtain the impedance properties of the corroding interface. The fitted EIS parameters are shown in **Supplemental Table S1**. Bode plots for the selected alloys passivated at 0.0V_{SCE} in 1 mM NaCl electrolyte are shown in **Fig. 7**. The Co-30Cr exhibited the highest low-frequency impedance magnitude of 10^6 Ω cm^2 while the other alloys displayed magnitudes greater than 3 x 10^5 Ω cm^2. The high low-frequency impedance magnitudes for each alloy suggest the formation of a relatively protective passive film.

The calculated oxide thickness as a function of time for each passive film is plotted in **Fig. 8.** The passive film on the Cr22- and Cr10-MPEA grew towards a steady state thickness of approximately 4 nm after 10ks. The Cr22-MPEAs passive film formed at a faster rate than the low Cr-MPEAs as indicated by a thicker layer at earlier passivation times with Cr10-MPEA exhibiting the slowest growth rate. All Cr-MPEAs oxide thicknesses approached a steady state value after approximately 6000 s. Compared to the binary alloys, Fe-20Cr was estimated to have similar passive film thickness as Cr22- and Cr10-MPEA (~ 4 nm). All other binary alloys showed a slightly thicker calculated passive film than the Cr-MPEAs.

The total electrochemical charge, ion ejection charge (q_{total} - q_{ox}), and charge efficiency associated with passivation as a function of bulk Cr content for each passive film formed during 10 ks potential hold are shown in **Fig. 9**. The total electrochemical charge and ion ejection charge decreased as Cr content increased in all tested alloys (**Figs. 9a** and **9b**). The charge efficiency for passivation, computed from q_{total} and q_{ox} given by Eq. 1, increased with bulk Cr concentrations (**Fig. 9c**) and nearly approached 1 for 30% Cr alloys. The Cr-MPEAs and binary

alloys follow the same trend with no distinction between MPEAs and binary alloys. Cr22-MPEA exhibited a lowered ion ejection charge and better efficiency than all other tested low Cr-alloys, as did the Ni-24Cr and Co-30Cr binary alloys. The Cr10-MPEA exhibited the highest ion ejection charge and lowest efficiency compared to all the other alloys, suggesting the greatest rate of ion dissolution to solution in contrast with joining the passive film among these alloys (**Fig. 9**). Ni-12Cr was the next highest in total electrochemical charge and ion ejection charge, and correspondingly the next lowest in efficiency. However, other low Cr alloys did not passivate and are therefore not included in this plot. It can be suspected that the trend for low efficiencies typical of 5, 6 and 10 at. % Cr alloys produce conditions where passivation cannot be achieved on these alloys in this electrolyte.

3.3. Oxide valence state and cation fractions identified by XPS

The chemical states and composition of the electrochemically formed passive films on the Cr-MPEAs and binary alloys were determined by XPS and are summarized in **Table 2**. Overall, all passive films contain a large amount of Cr(III), present as both oxide and hydroxide. The Cr-MPEAs passive films consisted mainly of Cr(III) and small amounts of Ni(II) and Fe(II) species. . Mn(II), Mn(III), and Co(II) $2p_{1/2}$ signals were not evident above the detection limit, suggesting that the Mn and Co species are either present in the oxides at very low levels or are not oxidized. This upper limit for Mn, ≤ 0.06 cation fraction, remains similar throughout the Cr-MPEA series even though the bulk Mn concentration increases with decreasing bulk Cr **(Table 2).** Conversely, the Co upper limit increases with decreasing bulk Cr concentrations. The Fe cation fraction remained constant for each Cr-MPEA. The Ni cation fraction of 0.07 was lowest in the Cr22-MPEA and increases to 0.14 for Cr14- and Cr10-MPEA. Cr22-MPEA exhibited a higher Cr concentration in the oxide/hydroxide passive layer compared to the binaries Fe-20Cr,

Ni-24Cr, and Ni-12Cr. The Co-30Cr and Co-20Cr had the highest Cr cation fraction of 0.93 and 0.89, respectively. This result agrees with the elemental *in-situ* elemental dissolution profile of Co-20Cr, investigated by atomic emission spectroelectrochemistry (AESEC) technique. During passivation at 0.0 V_{SCE} for 10 ks, Cr dissolution was below the detection limit whereas Co showed an initial dissolution transient (these results are shown in the **Supplemental Fig. S5**). These AESEC observations are in agreement with XPS findings in which passive films formed on Co-Cr binary alloys were primarily Cr(III) species (**Table 2**).

The elemental fractions within the altered metal zone beneath the passivating film were also determined by XPS, as shown in **Table 2**. The Cr-MPEAs and Ni-Cr binary alloys exhibited an enrichment of Ni with respect to bulk Ni concentrations. The Cr elemental fraction in the altered zone was similar to the bulk concentration for the Cr22- and Cr14-MPEAs, with elemental fractions of 0.25 and 0.16, respectively. In the case of the Cr10-MPEA, a clear depletion of Cr was observed with an elemental fraction of 0.04. Depletion of Fe, Mn, and Co was also observed in the altered zone for each Cr-MPEA (**Table 2**). The simpler binary alloys had Cr concentrations similar to their bulk Cr concentrations within the altered zone (**Table 2**).

Deconvolution of the XPS spectra was performed and the resulting fits are shown in **Fig. 10**. The observed binding energies were consistent with the oxidation states Ni(II), Cr(III), and Fe(II) for all Cr-MPEAs. The passive films for all of the alloys consisted of primarily of hydrated Cr(III) rather than anhydrous Cr(III) (i.e., $Cr(OH)_3$ versus Cr_2O_3, respectively) as shown in **Supplemental Table S3**. This is in agreement with O 1s spectra for each alloy, in which a large intensity for the hydroxide feature was observed **(Fig. 10)**. The hydroxide species was observed as the majority of the Cr(III) and Ni(II) cations. The Co-30Cr contained the largest fraction of anhydrous Cr(III) (0.24) with all other alloys having fractions $\leq$ 0.11 (**Table S3**). The

Cr-MPEAs also contained a small fraction of Cr(III) whose best fit was associated with Cr-spinels such as ($NiCr_2O_4$ and/or $FeCr_2O_4$), unlike the passive films of the binary alloys (**Fig. 9 and Table S3**).

3.4. Passive film and interface compositions from APT

To better understand the elemental distribution within the electrochemically formed passive film and within the altered zone (i.e., metal/film interface), APT was performed on Cr10-MPEA, Cr22-MPEA, Co-20Cr and Fe-20Cr after potentiostatic passivation in deaerated 1 mM NaCl + HCl at pH 4. Results on the latter three alloys are reported as supplemental information (**Fig. S1-S3 and S6-S9**). Concerning the Cr10-MPEA, good agreement between XPS and APT is seen. A large enrichment of Cr (0.68 ≤ Cr fraction) is observed in the outer layer (i.e., from 1.10 to 4.50 nm) of the passive film shown in **Fig. 11**, similar to the XPS results (**Table 2**). A depletion of Mn (0.04 ≤ Mn fraction) is observed within the inner oxide and altered metal zone (-1.90 to 1.10 nm). In the outer oxide, the Mn elemental fraction increases up to 0.21 initially but then decreases to 0.08. Overall, this is consistent with XPS results (**Table 2**). Enrichment of Ni is observed within the altered zone and inner oxide (0.50 ≤ Ni fraction). The elemental fraction of Ni begins to decreases throughout the inner and outer oxide, also consistent with XPS (**Table 2**). Slight depletion of Cr (0.09 ≤ Cr fraction) and Mn (0.06 ≤ Mn fraction) is indicated within the altered zone as their fractions were lower than the nominal alloy values.

3.5. Passive film and altered zone alloying element enrichment and depletion factors

Cr enrichment and depletion terms within the electrochemically formed passive film ($f_{Cr,ox}$) and altered zone ($f_{Cr,az}$) for each MPEA and binary alloy is summarized in **Fig. 12**. **Figure 12** shows f_{Cr} for both the altered zone (red symbols) and passive film (black symbols) as a function of the bulk Cr alloying content. The passive film $f_{Cr,ox}$ values indicated similar Cr

enrichment for all alloys at high bulk Cr content except for the case of the Fe-20Cr binary. The $f_{Cr,ox}$ ranged from 3.6 to 7.0 under the conditions described above. The enrichment factor, $f_{Cr,ox}$ is larger in the low-Cr containing alloys but this is also observed for both the MPEA and the binary alloys with the same or similar trend. Notably, Cr10-MPEA exhibited the highest Cr enrichment factor ($f_{Cr,ox}$ = 7.0). The binary alloys follow the same trend as the MPEAs but do not exceed an $f_{Cr.ox}$ of 5.7. For example, Ni-12Cr has a higher bulk Cr content than Cr10-MPEA but shows a lower passive film $f_{Cr,ox}$ value of 5.7 compared to 7.0. The elemental $f_{Cr,az}$ within the altered zone did not change in any perceptible manner which can be discerned, with the exception of Cr10-MPEA. The Cr10-MPEA had the largest depletion of Cr with an $f_{Cr.az}$ of 0.4 within the altered zone.

From enrichment and depletion terms, the expected Cr concentration within the passive film and altered zone as a function of various bulk Cr concentrations are shown in **Fig. 13**. The enrichment or depletion of Cr is indicated by lines above or below the dashed line. The dashed line corresponds to the condition when the Cr concentration within the passive film (X^{ox}) is equal to the bulk Cr content (X^{S}). Both XPS and APT enrichment curves predict Cr enrichment in the passive film and slight depletion in the altered zone. XPS enrichment curves predict a higher Cr concentration than APT (**Fig. 13**), which could be due to the low Cr concentration observed within the inner oxide (**Fig. 11**). Experimental cation fractions for binary alloys (**Table 2**) were plotted and compared to the computed MPEA enrichment and depletion curves. The Co-Cr binary alloys were above the enrichment curve while the Ni-Cr and Fe-Cr alloys were slightly below. Further work would be needed to clarify the behavior of Cr10-MPEA.

A hypothetical mass transport controlled Cr depletion zone depth for the Cr22-MPEA, Cr10-MPEA, Ni-24Cr, Fe-20Cr, and Co-20Cr binary alloys is shown in **Fig. 14**. Alloys are

particularly shown to exhibit a larger depletion zone when the charge efficiency is less than 100%. At high charge efficiencies, a depletion zone of below a single atomic layer might be expected. This phenomenon is represented in **Fig. 15**, where charge efficiency (ion dissolution) is represented as pink arrows and correlate to a certain Cr depletion zone depth in pink, called the altered zone. However, at efficiency values of 1.0 to 0.4, a depletion zone on the order of 0.3-2.5 nm is evident. The Cr22- and Cr10-MPEA showed a similar hypothetical depletion profile as the 20 at. % Fe-Cr and Co-Cr binary alloys (**Fig. 14**). The Ni-24Cr alloy is predicted to have the largest depletion zone at equivalent oxide efficiencies compared to the other alloys. This is likely due to the thicker Ni-24Cr passive film (7.9 nm at the end of the experiment in **Fig. 8**) compared to the other alloys and relatively high Cr content. Thus, no special difference in the depletion zone in MPEAs versus binary allows is suggested from this analysis, nor seen in APT nor XPS analysis and thus no difference in Cr oxide enrichment as a result of an altered zone can be claimed. It is noted that more sluggish diffusion would render enrichment more difficult and would favor a depletion profile while faster diffusion would replenish depletion profiles and aid Cr enrichment.

4. Discussion

4.1. Thermodynamics and kinetics of aqueous passivation of Cr-MPEAs and binary alloys

In transition metals or "d-block" (i.e., Cr, Mn, Fe, Co, Ni) MPEAs and binary alloys containing Cr and subjected to moderately oxidizing conditions, all alloying elements can be assumed to exist in an oxidized but metastable state when exposed to moderate potentials such as 0.0 V_{SCE}, when the environment is slightly acidic [35, 67]. In this study, alloys above 10 at. % Cr showed clear passivation behavior and binary alloys at 5, 6, and 10 at. % Cr did not by the criterion of passivation over 10 ks at 0.0 V_{SCE} (**Fig. 1, 5** and **6)**. 10Cr-MPEA was an exception

that remained passive after 10ks potentiostatic hold at 0.0 V_{SCE} experiment while the 10 at. % Cr binary Fe-Cr and Co-Cr alloys were not passive (**Fig. 1** and **6**). The oxide on the 10Cr-MPEA is quite complex (**Fig. 11 and Figs. S1 and S6**) with possible phase separated layers and/or solid solutions. However, despite this, the Cr(III) enrichment is similar to that of binary alloys. In this study, both d-block non-equiatomic MPEA and all binary alloys with Cr solute exhibited Cr enrichment with Cr(III) enrichment factors (f_{Cr}) ranging from 3 to 7 (**Fig. 12**), and the resulting Cr cation fraction within the oxide exceeded 0.6 in all alloys (**Table 2**). No special effect was indicated in Cr-MPEAs relative to binaries except the finding that Fe-Cr was less enriched. Moreover, other elements were not present in the oxide film or were sparingly present in the inner layer or outer layer (**Table 2**).

Predicting which species will reside in the passive film and which will dissolve into solution during aqueous passivation using thermodynamics and kinetic indicators is difficult when multiple elements are considered. Thermodynamic predictions can be made by utilizing oxide formation energies and potential-pH stability diagrams [35, 67]. Without direct consideration of potential and pH and other factors, limited insights can be gained from formation energies. Thermodynamic oxide/hydroxide/spinel formation energies suggest multiple oxides could exist, such as $NiCr_2O_4$ (-1269.1 kJ/mol [68]), Cr_2O_3 (-1058 kJ/mol), $Cr(OH)_3$ (-1064 kJ/mol), NiO (-211.7 kJ/mol), $Ni(OH)_2$ (-447.3 kJ/mol), Fe_2O_3 (-742.2 kJ/mol), CoO (-214 kJ/mol), MnO (-362.9 kJ/mol), and $FeCr_2O_4$ (-1343.8 kJ/mol) [69]. Because of their more negative free energies of formation, it can be expected that Cr-based oxides are more thermodynamically favored than stoichiometric Ni, Fe, Co and Mn oxides. They also would have a high driving force to form when considering the potential that might be established by a passivating cathodic reaction [70]. This is supported by the XPS studies of MPEA passive films,

where Cr-hydroxides and Cr-spinel features are more pronounced compared than Ni-oxides and Ni-hydroxides (**Fig. 10**). Unfortunately, these predications are limited because third element effects, formation of solid solution oxides on a host lattice, kinetic limitations, and preferential and/or selective dissolution are not factored into the analysis [14, 17, 71-74].

Utilizing potential-pH stability diagrams considering a solid solution, further predications can be made in which solid solution oxides and dissolution of alloying elements should be considered. Wang et al. constructed potential-pH stability diagram of both stoichiometric and non-stoichiometric oxides for the $Ni_{38}Fe_{20}Cr_{22}Mn_{10}Co_{10}$ MPEA [35]. At 0.0 V_{SCE} in 0.6 m NaCl pH 4 environment, the following are predicted to be stable: stoichiometric Fe_2O_3, Cr_2O_3 and a non-stoichiometric spinel and corundum solid solution oxide containing Fe and Cr (**Fig. S4**). Under the same conditions, all alloying elements are also predicated to be present as aqueous species in the electrolyte as Ni(II), Fe(II), Cr(III), Mn(II), and Co(II) ions [35]. In this work, XPS deconvolution indicates the following oxides have formed: Cr_2O_3, $Cr(OH)_3$, $FeCr_2O_4$, and $NiCr_2O_4$ (**Fig. 10**). Thermodynamics cannot forecast the results observed; although the potential-pH [35] approach offers the best hope. More factors must be considered to deal with the complexity of the system.

Solid solution oxides or complex oxides containing two or more elements are hard to detect experimentally via XPS because of uncertainty in the binding energies of core level electrons after a photoelectron is formed. These phases cannot be independently confirmed by XPS without structural information. Previous investigations of Cr22-MPEA have shown similar results at a more negative potential (-0.25 V_{SCE}) in 0.1 M NaCl pH 4 [54]. In that work, AESEC investigations on Cr22-MPEA showed congruent dissolution of Ni, Fe and Co and non-congruent dissolution of Cr and Mn at a passive potential of -0.25 V_{SCE} [54]. In the present work,

low oxide concentrations of Ni, Fe, Co, and Mn compared to Cr were characterized by XPS (**Fig. 10**) and APT (**Fig. 11**) after a potentiostatic hold experiment at 0.0 V_{SCE} in 1 mM NaCl pH 4 electrolyte. This result suggests that these elements have dissolved into the solution, which is consistent with the above thermodynamic predictions and previous Cr22-MPEA investigations [32, 54].

This behavior is expected. Consider pure metals and their passive behavior when polarized in a slightly acidic Cl^- aqueous environment. When polarized to positive potentials, Cr and Ni commonly show a passive potential region approximately between -0.5 to 0.5 V_{SCE} whereas Fe, Mn, and Co undergo active corrosion (i.e., no passive region). If the passive behavior of an MPEA is similar to the pure metal tendencies, then it would be predictable that the passive species (Cr, Ni) are enriched within a MPEA passive film. With this assumption, a correlation could be made between the stationary current density at the passive electrode potential of pure metals. Enrichment or depletion within oxide film can be estimated by Eq. 2;

$$f_{Cr} = \frac{i_{ss,Y}}{i_{ss.Cr}} \qquad (2)$$

where $i_{ss,Y}$ is the stationary current density at 0.0 V_{SCE} for the solvent element (considered to be pure Ni for the Cr-MPEAs) and $i_{ss,Cr}$ is the stationary current density of pure Cr at 0.0 V_{SCE} [72]. If the stationary current density of pure Cr is low and it is significantly higher in the other alloying elements, then enrichment occurs by the dissolution of the other alloying elements. This phenomenon could contribute to the low amounts of Fe, Mn, and Co within the passive films formed on the MPEAs at 0.0 V_{SCE} (**Table 2**). When polarized in deaerated 1 mM NaCl pH 4, pure Cr and Ni show passive potential regions with Cr possessing the lower passive current density at 0.0 V_{SCE} (~ 2 x 10^{-6} and 1 x 10^{-5} A cm^{-2}, respectively), as shown in **Supplemental Fig.**

S10. In the case of pure Fe, Mn, and Co, no clear passive potential region is observed and current densities are much higher (~5 x 10^{-5} to 10^{-4} A cm^2) than Cr and Ni. These stationary current densities all suggest Cr should be enriched within the passive film, and Fe, Mn, and Co are expected to dissolve into solution. This is indeed observed when considering the Cr22- and Cr14-MPEA passive film cation fractions (**Table 2**).

4.2. Other factors controlling Cr enrichment and depletion

An important question to address is what other factors limit Cr enrichment within the passive film? Kinetics are important because all alloying elements have a thermodynamic tendency for oxidation when these alloys are exposed in an oxidizing solution and this is not a discriminating factor. Meanwhile, non-congruent oxidation and chemical dissolution are likely and Cr enrichment may be enhanced by this process without theoretical limit. Moreover, the process of enriching from less than 10 at. % Cr in the alloy towards more than 60 cation % in a nm thick passive film also supports an unproven notion of fast transport in the solid solution. Cr must be supplied through the altered zone. Cr buildup in the passive film will also be influenced by inefficient Cr oxide formation (**Fig. 9** and **14**), considering that any Cr that dissolves into solution cannot contribute to oxide enrichment (**Fig. 15**). This effect can be observed in **Fig. 14**, which shows the effect of low charge efficiency on the formation of a depletion zone or altered zone below the passive film. Of the selected alloys passivated at 0.0 V_{SCE}, the Cr10-MPEA showed high Cr enrichment within the passive film, as well as depletion of Cr within the altered zone calculated from XPS and APT (**Fig. 10** and **11**), and low efficiency. These factors can limit Cr enrichment.

From XPS Cr enrichment and depletion factors ($f_{Cr,ox}$ and $f_{Cr,az}$), a comparison of enrichment or depletion within the altered zone can be made amongst both the binary alloys and MPEAs

after electrochemical passivation **(Fig. 12).** The Cr10-MPEA showed a depletion of Cr within the altered zone, whereas Cr depletion could not be detected via XPS in other alloys **(Fig. 12** and **Table 2).** Besides the depletion argument which is not informed by enough data to conclude that it limits Cr enrichment in the passive film, the best argument for enrichment is that it is enabled by selective dissolution of other alloying elements during potentiostatic passivation at 0.0 V_{SCE} [21, 27, 28, 32, 51].

From the kinetic viewpoint, Fe, Co, and Mn are likely selectively depleted in the tested condition [54]. If these alloying elements are selectively dissolved, then Cr is left behind eventually creating "clusters" of Cr, available to be oxidized and inter-connected. The availability of these Cr clusters to form will depend on the bulk alloy Cr concentration, solid state diffusion, surface diffusion, ordered, random or clustered Cr and how likely other alloying elements will dissolve into solution [21, 28]. For random solid solutions at Cr bulk concentrations ≥ 14 at. % and Mn and Co bulk content of ≤ 14 at. %, there is an increase in the probability of Cr atoms surrounding each other rather than being surrounded by Mn or Co atoms. At bulk Cr concentrations ≤ 10 at. %, and Mn and Co bulk content ≥ 16 at. %, the reverse happens and Cr is more likely to be nearest neighbors with nearby Mn and Co rather than a Cr atom. Due to this situation, more bulk material would need to dissolve to supply enough Cr to form a uniform nm thick passive film. Once the oxide covers the surface, Cr is predicted to enrich.

Even with an altered zone, high Cr enrichment within the passive film is suggested for the Cr10-MPEA and this phenomenon might also be correlated to various atomistic properties such as cohesive energy and diffusion rates [75]. The diffusion process of an equiatomic FeNiCrCoCu FCC alloy was investigated by modeling of various atomic properties and then comparison to

pure metals [75]. Correlations were observed with cohesive and vacancy formation energies. Diffusion rates were faster for elements with lower cohesive and vacancy formation energies (e.g., pure Cr and Fe with a cohesive energy of 4.2 eV and 4.4 eV, respectively) [75]. Cr was observed to have a faster diffusion rate both in pure Cr and the FeNiCrCoCu alloy compared to Fe. This could be correlated to the lower cohesive energy of Cr. Moreover, if Cr diffuses faster than other alloying elements, it could readily provide a supply of Cr to the altered zone for continued Cr oxidation. It remains to be determined whether MPEAs can enable faster Cr diffusion in the altered zone than binary alloys. However, the MPEA with 10 at. % Cr investigated in this work exhibited passivation, with strong Cr enrichment in the passive film and a small amount of Cr depletion within the altered zone. Other factors could contribute to the observed enrichment and depletion of Cr in the altered zone, such as grain boundary diffusion or altered vacancy mediated diffusion [75-77]. These factors should be considered in future work.

5. Conclusions

Electrochemical passivation of Cr-MPEAs containing Fe, Mn, Co and Ni was investigated over a range of Cr concentrations from 6.0 to 22 at. % and compared to binary Ni-Cr, Fe-Cr, and Co-Cr alloys with similar bulk Cr concentrations. The following conclusions can be drawn:

- LSV experiments revealed well-defined passive potential regions for the MPEAs alloys with bulk Cr concentration ≥ 10 at. % and for Ni-Cr ≥ 12% Cr. The Cr6-MPEA, Fe-xCr, Ni-xCr, and Co-xCr (x ≤10 at. %) had limited passivity and underwent localized crevice corrosion. Notably, the MPEA alloy with 10% Cr was shown to have lower sustained passive current densities compared to binary alloys with 10% Cr.
- Alloys that showed significant passivation behavior during 10 ks potentiostatic hold experiment at 0.0 VSCE in 1 mM NaCl pH 4 formed a passive film enriched with Cr(III)

species at cation fractions well above the bulk Cr content in the alloy. The Cr10-MPEA showed the highest passive film Cr enrichment factor ($f_{Cr,ox}$) of 7.0 compared to all other alloys investigated in this work but passivation efficiency and enrichment factor was consistent with the trends observed for binary alloys except for Fe-Cr.

- The passive film for all alloys consisted mainly of hydrous Cr(III) with small amounts of anhydrous Cr(III). The passive films of the Cr-MPEAs were also suggested to have small amounts of Cr-spinels with Ni or Fe, while these species were not detected in the passive films formed on the binary alloys.
- Cr depletion within the altered zone at the metal/oxide interface and the solid state diffusion rates of Cr should be consider as potential limiting factors in Cr oxide enrichment and not be neglected in aqueous passivation models. Cr supply to oxides could be enabled by an alloy composition enabling enhanced vacancy assisted solid state diffusion of Cr which has been observed on similar alloys.
- The reported Cr enrichment within the electrochemically formed passive films was attributed mainly to the selective dissolution of Ni, Fe, Mn, and Co. Moreover, the enrichment factor for Cr(III) could not be uniquely associated with and special alloying "third element effects" based on Ni, Co, Mn or Fe alloying elements.

Acknowledgements

This work was supported as part of the Center for Performance and Design of Nuclear Waste Forms and Containers, an Energy Frontier Research Center funded by the U.S. Department of Energy (DOE), Office of Science, Basic Energy Sciences under Award #DE-SC0016584. PHI VersaProbe III system was supported by NSF Award 162601, MRI Acquisition of an X-Ray Photoelectron Spectrometer for Chemical Mapping of Evolving Surfaces: A Regional Instrument for Research and Teaching. DKS and LJK acknowledge support from the U.S. DOE, Office of Science, Basic Energy Sciences, Materials Science and Engineering Division for performing

APT measurements. A portion of this research was performed on a project award (10.46936/cpcy.proj.2021.60217/600007228) from the Environmental Molecular Sciences Laboratory, a DOE Office of Science User Facility sponsored by the Biological and Environmental Research program and located at Pacific Northwest National Laboratory (PNNL). PNNL is a multiprogram national laboratory operated by Battelle for the U.S. DOE under Contract DE-AC05-76RLO1830. K. Ogle and the AESEC experiments conducted by J. Han were supported by the Agence Nationale de Recherche, grant # ANR-20-CE08-0031 (TAPAS 2020).

Table 1.
Multiple-Principal Element Alloys and Binary Alloys Composition

Alloy	**Nominal Chemical Composition (at. %)**
Cr22-MPEA*	38Ni-20Fe-22Cr-10Mn-10Co
Cr14-MPEA*	38Ni-20Fe-14Cr-14Mn-14Co
Cr10-MPEA*	38Ni-20Fe-10Cr-16Mn-16Co
Cr6-MPEA**	38Ni-20Fe-6Cr-14Mn-14Co
Fe-30Cr	70Fe-30Cr (72.4Fe-27.6Cr)
Fe-20Cr*	80Fe-20Cr (80.8Fe-19.2Cr)
Fe-10Cr	90Fe-10Cr (87.2Fe-12.8Cr)
Fe-5Cr	95Fe-5Cr (95.1Fe-4.9Cr)
Co-30Cr*	70Co-30Cr (70.0Co-30.0Cr)
Co-20Cr*	80Co-20Cr (78.9Co-21.1Cr)
Co-10Cr**	90Co-10Cr (91.2Co-8.8Cr)
Co-5Cr	95Co-5Cr (95.6Co-4.4Cr)
Ni-30Cr	70Ni-30Cr
Ni-20Cr	80Ni-20Cr
Ni-10Cr	90Ni-10Cr
Ni-5Cr	95Ni-5Cr
Ni-24Cr*	76Ni-24Cr
Ni-12Cr*	88Ni-12Cr

(*) alloys passivated at 0 V_{SCE} and resulting film characterized
(**) alloys initially passive but broke down during 10ks oxide growth at 0 V_{SCE}
(Elemental Composition determined by Energy Dispersive X-ray Spectroscopy)

Table 2.
All cation and elemental fractions detected by XPS for passive films formed at 0.0 V_{SCE} for 10 ks in 1 mM NaCl + HCl pH 4 $N_{2(g)}$ deaerated solution and within the altered zone.

Alloy	Passive Film Cation Fraction	Altered Zone Elemental Fraction

	Ni(II)	Fe(II)	Cr(III)	Mn(II)	Co(II)	Ni	Fe	Cr	Mn	Co
Cr22-MPEA	0.07	0.07	0.8	0.02*	0.04*	0.57	0.12	0.25	0.03*	0.03*
Cr14-MPEA	0.14	0.07	0.71	0.02*	0.06*	0.64	0.13	0.16	0.03*	0.04*
Cr10-MPEA	0.14	0.07	0.70	0.01*	0.08*	0.77	0.06	0.04	0.06*	0.07*
Fe-20Cr	--	0.23	0.77	--	--	--	0.82	0.18	--	--
Co-30Cr	--	--	0.93	--	0.07	--	--	0.28	--	0.72
Co-20Cr	--	--	0.89	--	0.11	--	--	0.20	--	0.80
Ni-24Cr	0.27	--	0.73	--	--	0.74	--	0.26	--	--
Ni-12Cr	0.31	--	0.69	--	--	0.89	--	0.11	--	--

*Assuming max allowed Mn and Co fractions consistent with XPS $2p_{1/2}$ signal.

References

[1] K. Asami, K. Hashimoto, T. Masumoto, S. Shimodaira, ESCA study of the passive film on an extremely corrosion-resistant amorphous iron alloy, Corrosion Science 16(12) (1976) 909-914.
[2] K.L. Cwalina, H.M. Ha, N. Ott, P. Reinke, N. Birbilis, J.R. Scully, In Operando Analysis of Passive Film Growth on Ni-Cr and Ni-Cr-Mo Alloys in Chloride Solutions, Journal of The Electrochemical Society 166(11) (2019) C3241-C3253.
[3] S.-P. Jeng, P.H. Holloway, C.D. Batich, Surface passivation of Ni/Cr alloy at room temperature, Surface Science 227(3) (1990) 278-290.
[4] I. Olefjord, H. Fischmeister, ESCA studies of the composition profile of low temperature oxide formed on chromium steels—II. Corrosion in oxygenated water, Corrosion Science 15(6) (1975) 697-707.
[5] K. Asami, K. Hashimoto, S. Shimodaira, An XPS study of the passivity of a series of iron—chromium alloys in sulphuric acid, Corrosion Science 18(2) (1978) 151-160.
[6] A.P. Bond, H.H. Uhlig, Corrosion Behavior and Passivity of Nickel-Chromium and Cobalt-Chromium Alloys, Journal of The Electrochemical Society 107(6) (1960) 488.
[7] P.F. King, H.H. Uhlig, Passivity in the Iron-Chromium Binary Alloys, The Journal of Physical Chemistry 63(12) (1959) 2026-2032.
[8] E. McCafferty, Graph theory and the passivity of binary alloys, Corrosion Science 42(11) (2000) 1993-2011.
[9] E. McCafferty, Relationship Between Graph Theory and Percolation Approaches in the Passivity of Fe–Cr Binary Alloys, Journal of The Electrochemical Society 155(10) (2008) C501-C505.
[10] H.H. Uhlig, G.E. Woodside, Anodic Polarization of Passive and Non-passive Chromium–Iron Alloys, The Journal of Physical Chemistry 57(3) (1953) 280-283.
[11] X.M. Zhu, Y.S. Zhang, Investigation of the Electrochemical Corrosion Behavior and Passive Film for Fe-Mn, Fe-Mn-Al, and Fe-Mn-Al-Cr Alloys in Aqueous Solutions, CORROSION 54(1) (1998) 3-12.
[12] C.R. Clayton, A Bipolar Model of the Passivity of Stainless Steel: The Role of Mo Addition, Journal of The Electrochemical Society 133(12) (1986) 2465.
[13] P. Jakupi, D. Zagidulin, J.J. Noël, D.W. Shoesmith, The impedance properties of the oxide film on the Ni–Cr–Mo Alloy-22 in neutral concentrated sodium chloride solution, Electrochimica Acta 56(17) (2011) 6251-6259.

[14] A.C. Lloyd, J.J. Noël, S. McIntyre, D.W. Shoesmith, Cr, Mo and W alloying additions in Ni and their effect on passivity, Electrochimica Acta 49(17) (2004) 3015-3027.
[15] A.C. Lloyd, J.J. Noël, D.W. Shoesmith, N.S. McIntyre, The open-circuit ennoblement of alloy C-22 and other Ni-Cr-Mo alloys, JOM 57(1) (2005) 31-35.
[16] K. SUGIMOTO, Y. SAWADA, The Role of Alloyed Molybdenum in Austenitic Stainless Steels in the Inhibition of Pitting in Neutral Halide Solutions, CORROSION 32(9) (1976) 347-352.
[17] X. Zhang, D. Zagidulin, D.W. Shoesmith, Characterization of film properties on the NiCrMo Alloy C-2000, Electrochimica Acta 89 (2013) 814-822.
[18] E. McCafferty, Oxide networks, graph theory, and the passivity of Ni–Cr–Mo ternary alloys, Corrosion Science 50(12) (2008) 3622-3628.
[19] K. Osozawa, H.J. Engell, The anodic polarization curves of iron-nickel-chromium alloys, Corrosion Science 6(8) (1966) 389-393.
[20] E. McCafferty, Introduction to Corrosion Science, Springer, 233 Spring St, New York, NY 10013 USA, 2010.
[21] S. Qian, R.C. Newman, R.A. Cottis, K. Sieradzki, Validation of a Percolation Model for Passivation of Fe- Cr Alloys: Two- Dimensional Computer Simulations, Journal of The Electrochemical Society 137(2) (1990) 435-439.
[22] E. McCafferty, Oxide networks, graph theory, and the passivity of binary alloys, Corrosion Science 44(7) (2002) 1393-1409.
[23] E. McCafferty, Graph Theory and the Passivity of Iron-Chromium Binary Alloys, Electrochemical and Solid-State Letters 3(1) (2000) 28.
[24] E. McCafferty, General Relations Regarding Graph Theory and the Passivity of Binary Alloys, Journal of The Electrochemical Society 150(5) (2003) B238.
[25] E. McCafferty, Graph theory and binary alloys passivated by nickel, Corrosion Science 47(7) (2005) 1765-1777.
[26] P.C. Searson, R. Li, K. Sieradzki, Surface Diffusion in the Solid-on-Solid Model, Physical Review Letters 74(8) (1995) 1395-1398.
[27] K. Sieradzki, R.C. Newman, A Percolation Model for Passivation in Stainless Steels, Journal of The Electrochemical Society 133(9) (1986) 1979-1980.
[28] Y. Xie, D.M. Artymowicz, P.P. Lopes, A. Aiello, D. Wang, J.L. Hart, E. Anber, M.L. Taheri, H. Zhuang, R.C. Newman, K. Sieradzki, A percolation theory for designing corrosion-resistant alloys, Nature Materials 20(6) (2021) 789-793.
[29] B.O. Elfström, The effect of chloride ions on passive layers on stainless steels, Materials Science and Engineering 42 (1980) 173-180.
[30] J.J. Gray, J.R. Hayes, G.E. Gdowski, B.E. Viani, C.A. Orme, Influence of Solution pH, Anion Concentration, and Temperature on the Corrosion Properties of Alloy 22, Journal of The Electrochemical Society 153(3) (2006) B61.
[31] J.J. Gray, C.A. Orme, Electrochemical impedance spectroscopy study of the passive films of alloy 22 in low pH nitrate and chloride environments, Electrochimica Acta 52(7) (2007) 2370-2375.
[32] J. Han, X. Li, A.Y. Gerard, P. Lu, J.E. Saal, G.S. Frankel, K. Ogle, J.R. Scully, Potential Dependent Mn Oxidation and Its Role in Passivation of Ni38Fe20Cr22Mn10Co10 Multi-Principal Element Alloy Using Multi-Element Resolved Atomic Emission Spectroelectrochemistry, Journal of The Electrochemical Society 168(5) (2021) 051508.

[33] X.Q. Wu, S. Xu, J.B. Huang, E.H. Han, W. Ke, K. Yang, Z.H. Jiang, Uniform corrosion and intergranular corrosion behavior of nickel-free and manganese alloyed high nitrogen stainless steels, Materials and Corrosion 59(8) (2008) 676-684.
[34] K. Park, H. Kwon, Effects of Mn on the localized corrosion behavior of Fe–18Cr alloys, Electrochimica Acta 55(9) (2010) 3421-3427.
[35] K. Wang, J. Han, A.Y. Gerard, J.R. Scully, B.-C. Zhou, Potential-pH diagrams considering complex oxide solution phases for understanding aqueous corrosion of multi-principal element alloys, npj Materials Degradation 4(1) (2020) 35.
[36] G. Wranglen, Pitting and sulphide inclusions in steel, Corrosion Science 14(5) (1974) 331-349.
[37] E.G. Webb, T. Suter, R.C. Alkire, Microelectrochemical Measurements of the Dissolution of Single MnS Inclusions, and the Prediction of the Critical Conditions for Pit Initiation on Stainless Steel, Journal of The Electrochemical Society 148(5) (2001) B186.
[38] S. Fajardo, I. Llorente, J.A. Jiménez, J.M. Bastidas, D.M. Bastidas, Effect of Mn additions on the corrosion behaviour of TWIP Fe-Mn-Al-Si austenitic steel in chloride solution, Corrosion Science 154 (2019) 246-253.
[39] T.D. Nguyen, J. Zhang, D. Young, Effect of Mn on oxide formation by Fe-Cr and Fe-Cr-Ni alloys in dry and wet CO 2 gases at 650°C, Corrosion Science 112 (2016) 110-127.
[40] A. Pardo, E. Otero, M.C. Merino, M.D. López, M.V. Utrilla, F. Moreno, Influence of pH and Chloride Concentration on the Pitting and Crevice Corrosion Behavior of High-Alloy Stainless Steels, CORROSION 56(4) (2000) 411-418.
[41] D.B. Miracle, O.N. Senkov, A critical review of high entropy alloys and related concepts, Acta Materialia 122 (2017) 448-511.
[42] A. Rodriguez, J.H. Tylczak, M. Ziomek-Moroz, Corrosion Behavior of CoCrFeMnNi High-Entropy Alloys (HEAs) Under Aqueous Acidic Conditions, ECS Transactions 77(11) (2017) 741-752.
[43] D.H. Xiao, P.F. Zhou, W.Q. Wu, H.Y. Diao, M.C. Gao, M. Song, P.K. Liaw, Microstructure, mechanical and corrosion behaviors of AlCoCuFeNi-(Cr,Ti) high entropy alloys, Materials & Design 116 (2017) 438-447.
[44] S. Yang, W. Yu, T. Liu, C. Li, Y. Zhang, Y. Qu, Effect of Cr content on corrosion behavior of AlCr x FeNi2Cu1.6 high entropy alloys, Materials Research Express 6(7) (2019) 076501.
[45] G.Y. Koga, N. Birbilis, G. Zepon, C.S. Kiminami, W.J. Botta, M. Kaufman, A. Clarke, F.G. Coury, Corrosion resistant and tough multi-principal element Cr-Co-Ni alloys, Journal of Alloys and Compounds 884 (2021) 161107.
[46] W. Chai, T. Lu, Y. Pan, Corrosion behaviors of FeCoNiCrx (x = 0, 0.5, 1.0) multi-principal element alloys: Role of Cr-induced segregation, Intermetallics 116 (2020) 106654.
[47] K.-M. Hsu, S.-H. Chen, C.-S. Lin, Microstructure and corrosion behavior of FeCrNiCoMnx (x = 1.0, 0.6, 0.3, 0) high entropy alloys in 0.5 M H2SO4, Corrosion Science 190 (2021) 109694.
[48] J. Yang, J. Wu, C.Y. Zhang, S.D. Zhang, B.J. Yang, W. Emori, J.Q. Wang, Effects of Mn on the electrochemical corrosion and passivation behavior of CoFeNiMnCr high-entropy alloy system in H2SO4 solution, Journal of Alloys and Compounds 819 (2020) 152943.
[49] L. Wang, D. Mercier, S. Zanna, A. Seyeux, M. Laurent-Brocq, L. Perrière, I. Guillot, P. Marcus, Study of the surface oxides and corrosion behaviour of an equiatomic CoCrFeMnNi high entropy alloy by XPS and ToF-SIMS, Corrosion Science 167 (2020) 108507.

[50] H. Luo, Z. Li, A.M. Mingers, D. Raabe, Corrosion behavior of an equiatomic CoCrFeMnNi high-entropy alloy compared with 304 stainless steel in sulfuric acid solution, Corrosion Science 134 (2018) 131-139.
[51] S.B. Inman, J. Han, A.Y. Gerard, J. Qi, M.A. Wischhusen, S.R. Agnew, S.J. Poon, K. Ogle, J.R. Scully, Effect of Mn Content on the Passivation and Corrosion of Al0.3Cr0.5Fe2MnxMo0.15Ni1.5Ti0.3 Compositionally Complex Face-Centered Cubic Alloys, Corrosion 78(1) (2021) 32-48.
[52] P. Lu, J.E. Saal, G.B. Olson, T. Li, S. Sahu, O.J. Swanson, G.S. Frankel, A.Y. Gerard, J.R. Scully, Computational design and initial corrosion assessment of a series of non-equimolar high entropy alloys, Scripta Materialia 172 (2019) 12-16.
[53] S. Sahu, O.J. Swanson, T. Li, A.Y. Gerard, J.R. Scully, G.S. Frankel, Localized Corrosion Behavior of Non-Equiatomic NiFeCrMnCo Multi-Principal Element Alloys, Electrochimica Acta 354 (2020) 136749.
[54] A.Y. Gerard, J. Han, S.J. McDonnell, K. Ogle, E.J. Kautz, D.K. Schreiber, P. Lu, J.E. Saal, G.S. Frankel, J.R. Scully, Aqueous passivation of multi-principal element alloy Ni38Fe20Cr22Mn10Co10: Unexpected high Cr enrichment within the passive film, Acta Materialia 198 (2020) 121-133.
[55] E.J. Kautz, S.V. Lambeets, D.E. Perea, A.Y. Gerard, J. Han, J.R. Scully, J.E. Saal, D.K. Schreiber, Element redistributions during early stages of oxidation in a Ni38Cr22Fe20Mn10Co10 multi-principal element alloy, Scripta Materialia 194 (2021) 113609.
[56] S.M. Bruemmer, M.J. Olszta, M.B. Toloczko, D.K. Schreiber, Grain boundary selective oxidation and intergranular stress corrosion crack growth of high-purity nickel binary alloys in high-temperature hydrogenated water, Corrosion Science 131 (2018) 310-323.
[57] K. Lutton, K. Gusieva, N. Ott, N. Birbilis, J.R. Scully, Understanding multi-element alloy passivation in acidic solutions using operando methods, Electrochemistry Communications 80 (2017) 44-47.
[58] K. Gusieva, K.L. Cwalina, W.H. Blades, G. Ramalingam, J.H. Perepezko, P. Reinke, J.R. Scully, Repassivation Behavior of Individual Grain Facets on Dilute Ni–Cr and Ni–Cr–Mo Alloys in Acidified Chloride Solution, The Journal of Physical Chemistry C 122(34) (2018) 19499-19513.
[59] K.F. Quiambao, S.J. McDonnell, D.K. Schreiber, A.Y. Gerard, K.M. Freedy, P. Lu, J.E. Saal, G.S. Frankel, J.R. Scully, Passivation of a corrosion resistant high entropy alloy in non-oxidizing sulfate solutions, Acta Materialia 164 (2019) 362-376.
[60] T. Li, O.J. Swanson, G.S. Frankel, A.Y. Gerard, P. Lu, J.E. Saal, J.R. Scully, Localized corrosion behavior of a single-phase non-equimolar high entropy alloy, Electrochimica Acta 306 (2019) 71-84.
[61] S. Doniach, M. Sunjic, Many-electron singularity in X-ray photoemission and X-ray line spectra from metals, Journal of Physics C: Solid State Physics 3(2) (1970) 285-291.
[62] KOLXPD, http://kolxpd.kolibrik.net.
[63] M.C. Biesinger, B.P. Payne, A.P. Grosvenor, L.W.M. Lau, A.R. Gerson, R.S.C. Smart, Resolving surface chemical states in XPS analysis of first row transition metals, oxides and hydroxides: Cr, Mn, Fe, Co and Ni, Applied Surface Science 257(7) (2011) 2717-2730.
[64] K. Thompson, D. Lawrence, D.J. Larson, J.D. Olson, T.F. Kelly, B. Gorman, In situ site-specific specimen preparation for atom probe tomography, Ultramicroscopy 107(2) (2007) 131-139.

[65] J.E. Castle, K. Asami, A more general method for ranking the enrichment of alloying elements in passivation films, Surface and Interface Analysis 36(3) (2004) 220-224.
[66] H.E. Evans, Cavity formation and metallurgical changes induced by growth of oxide scale, Materials Science and Technology 4(12) (1988) 1089-1098.
[67] M. Pourbaix, Atlas of Electrochemical Equilibria in Aqeous Solutions National Association of Corrosion Engineers, Houston, TX, 1974.
[68] Y. Jiao, S. Zhang, Y. Tan, Thermodynamic Analysis and Crystallographic Properties of MFe2O4, MCr2O4 and MAl2O4 (M = Fe, Ni, Zn) Formed on Structural Materials in Pressurized Water Reactor Primary Circuit under Zinc and Zinc-aluminum Water Chemistry, Entropy 24(2) (2022) 245.
[69] J.G.S.a.N.A. Lange, Lange's Handbook of Chemistry McGraw-Hill Education, New York, 2017.
[70] L.N. Walters, E.L. Wang, J.M. Rondinelli, Thermodynamic Descriptors to Predict Oxide Formation in Aqueous Solutions, The Journal of Physical Chemistry Letters 13(26) (2022) 6236-6243.
[71] P. Marcus, J.M. Grimal, The anodic dissolution and passivation of NiCrFe alloys studied by ESCA, Corrosion Science 33(5) (1992) 805-814.
[72] R. Kirchheim, B. Heine, H. Fischmeister, S. Hofmann, H. Knote, U. Stolz, The passivity of iron-chromium alloys, Corrosion Science 29(7) (1989) 899-917.
[73] C.S. Giggins, F.S. Pettit, Oxidation of Ni-Cr-Al Alloys Between 1000° and 1200°C, Journal of The Electrochemical Society 118(11) (1971) 1782.
[74] W.J. Nowak, B. Wierzba, J. Sieniawski, Effect of Ti and Ta on Oxidation Kinetic of Chromia Forming Ni-Base Superalloys in Ar-O2-Based Atmosphere, High Temperature Materials and Processes 37(9-10) (2018) 801-806.
[75] A. Seoane, D. Farkas, X.-M. Bai, Influence of compositional complexity on species diffusion behavior in high-entropy solid-solution alloys, Journal of Materials Research 37(7) (2022) 1403-1415.
[76] V. Alexandrov, M.L. Sushko, D.K. Schreiber, S.M. Bruemmer, K.M. Rosso, Ab Initio Modeling of Bulk and Intragranular Diffusion in Ni Alloys, The Journal of Physical Chemistry Letters 6(9) (2015) 1618-1623.
[77] G. Laplanche, S. Berglund, C. Reinhart, A. Kostka, F. Fox, E.P. George, Phase stability and kinetics of σ-phase precipitation in CrMnFeCoNi high-entropy alloys, Acta Materialia 161 (2018) 338-351.

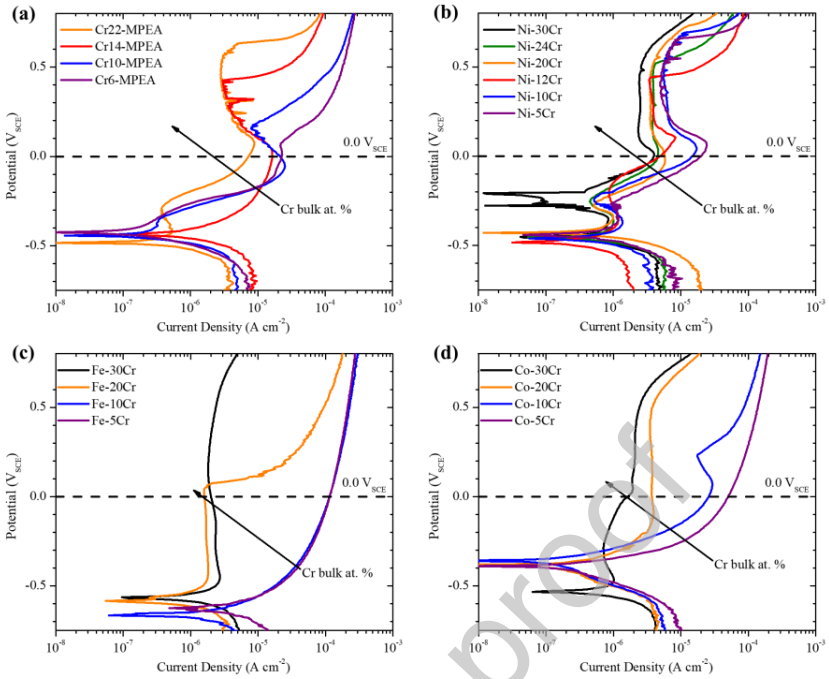

Fig. 1. Linear sweep voltammetry in $N_{2(g)}$ deaerated 1 mM NaCl + HCl electrolyte at pH 4 after initial cathodic reduction at -1.3 V_{SCE} for 600 s for **(a)** Cr-MPEAs, **(b)** Ni-xCr binary alloys (x = 30, 20, 24, 12, 10, 5 Cr atomic %), **(c)** Fe-*x*Cr binary alloys and **(d)** Co-xCr binary alloys. Where x = 30, 20, 10, 5 Cr at. %.

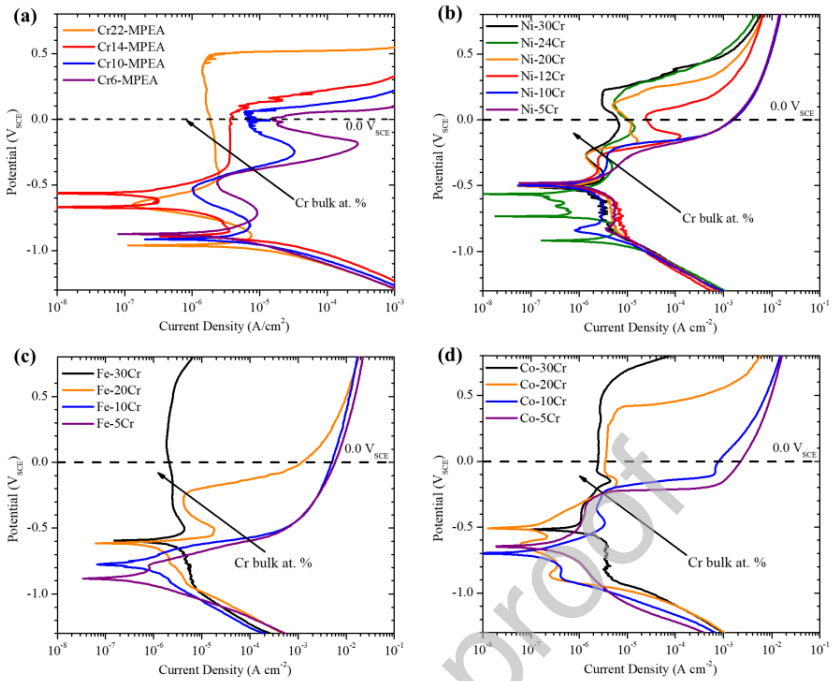

Fig. 2. Linear sweep voltammetry in $N_{2(g)}$ deaerated 0.1 M NaCl + HCl at pH 4 after initial cathodic reduction at -1.3 V_{SCE} for 600 s for **(a)** Cr-MPEAs, **(b)** Ni-xCr binary alloys (x = 30, 20, 24, 12, 10, 5 Cr atomic %), **(c)** Fe-xCr binary alloys and **(d)** Co-xCr binary alloys. Where x = 30, 20, 10, 5 Cr at. %.

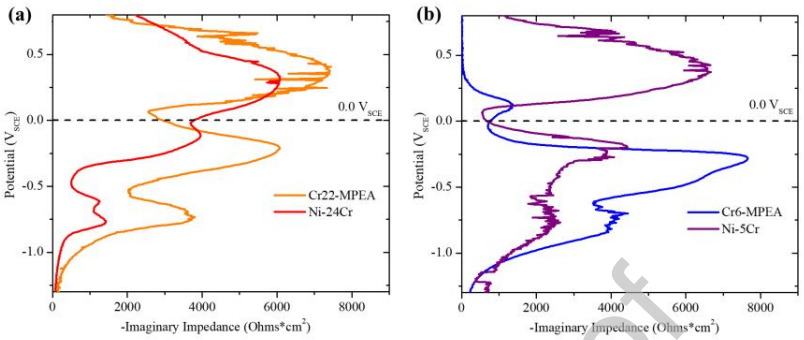

Fig. 3. Potential vs. imaginary component of impedance (-Z") at *f* = Hz during LSV with 0.5 mV s^{-1} scan rate in $N_{2(g)}$ deaerated 1 mM NaCl + HCl at pH 4 after initial cathodic reduction at -1.3V_{SCE} for 600 s for **(a)** Cr22-MPEA versus Ni-24Cr, and **(b)** Cr6-MPEA versus Ni-5Cr

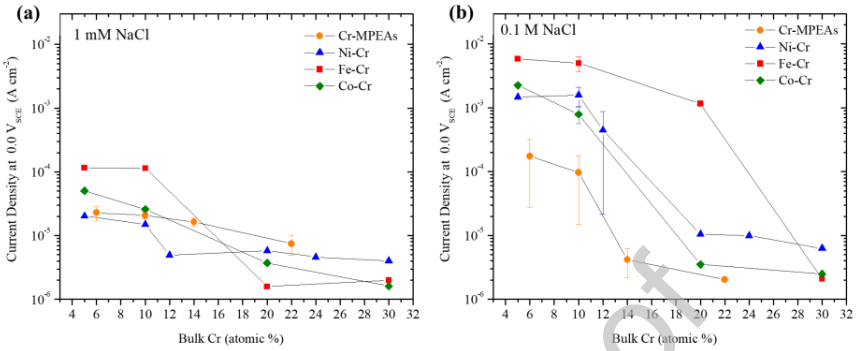

Fig. 4. Comparison of current density versus bulk alloy Cr concentration at 0.0 V_{SCE} acquired from linear sweep voltammetry for Cr-MPEAs, Ni-Cr, Fe-Cr, and Co-Cr alloys in **(a)** $N_{2(g)}$ deaerated 1 mM NaCl + HCl at pH 4 and **(b)** $N_{2(g)}$ deaerated 0.1 M NaCl + HCl at pH 4. Standard errors bars were computed from repeated experiments.

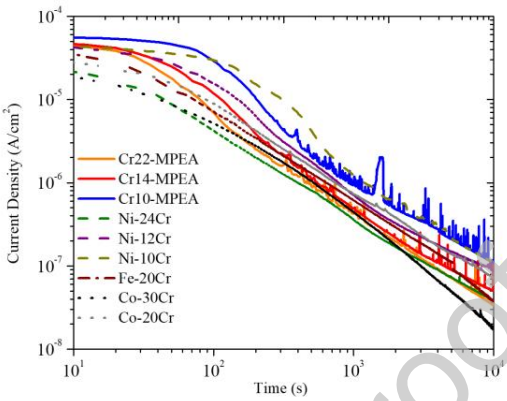

Fig. 5. Measured electrochemical current density during potentiostatic hold at 0.0 V_{SCE} for 10 ks 4 after initial cathodic reduction at -1.3 V_{SCE} for 600 s in deaerated 1 mM NaCl + HCl at pH 4 of Cr22-MPEA, Cr14-MPEA, Cr10-MPEA, Ni-24Cr, Ni-12Cr, Ni-10Cr, Fe-20Cr, Co-30Cr, and Co-20Cr.

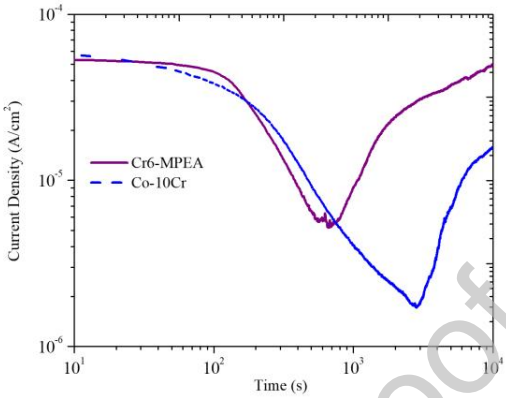

Fig. 6. Measured electrochemical current density during potentiostatic hold at 0.0 V_{SCE} for 10 ks 4 after initial cathodic reduction at -1.3V_{SCE} for 600 s in deaerated 1 mM NaCl + HCl at pH 4 of Cr6-MPEA and Co-10Cr.

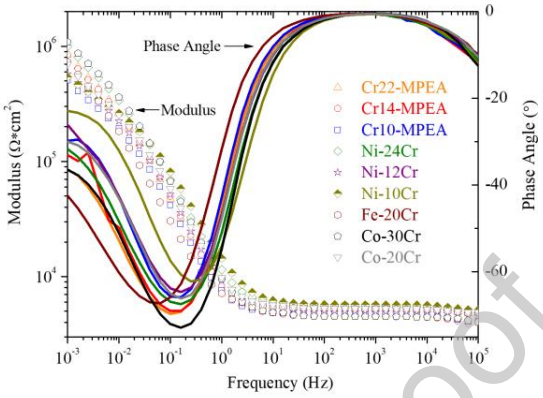

Fig. 7. Bode plot of Cr22-MPEA, Cr14-MPEA, Cr10-MPEA, Ni-24Cr, Ni-12Cr, Ni-10Cr, Fe-20Cr, Co-30Cr, and Co-20Cr in deaerated 1 mM NaCl + HCl at pH 4 after potentiostatic hold at 0.0 V_{SCE} for 10 ks.

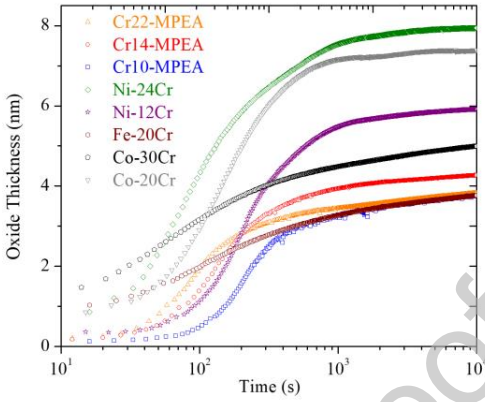

Fig. 8. In-situ estimation of oxide thickness for Cr22-MPEA, Cr14-MPEA, Cr10-MPEA, Ni-24Cr, Ni-12Cr, Fe-20Cr, Co-30Cr, and Co-20Cr during potentiostatic hold at 0.0 V_{SCE} for 10 ks in deaerated 1 mM NaCl + HCl at pH 4.

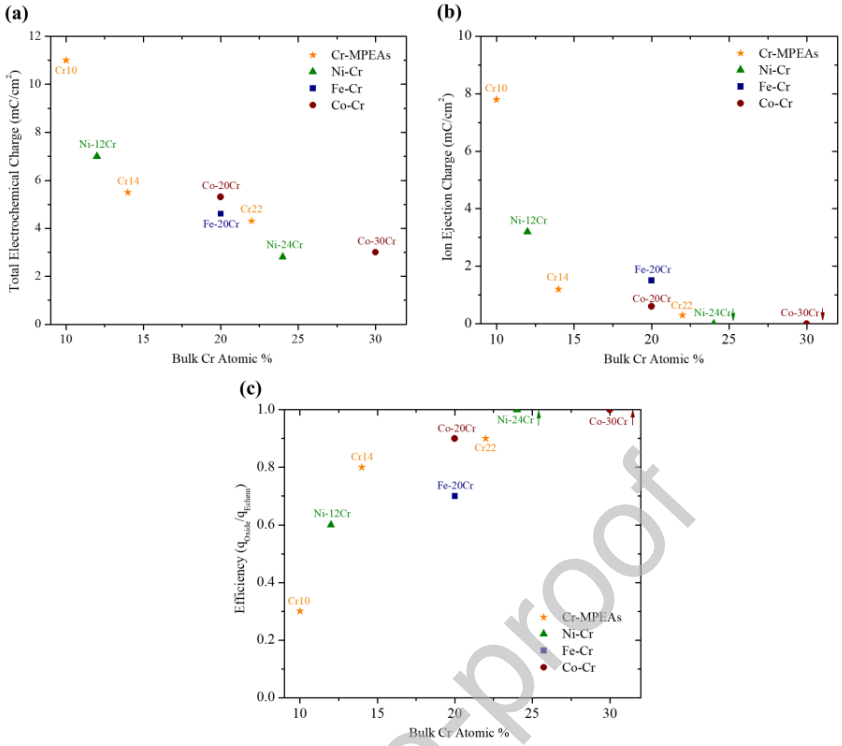

Fig. 9. (a) Total electrochemical charge, **(b)** ion ejection charge, and **(c)** efficiency of passive films formed on Cr22-MPEA, Cr14-MPEA, Cr10-MPEA, Ni-24Cr, Ni-12Cr, Fe-20Cr, Co-30Cr, and Co-20Cr during potentiostatic hold at 0.0 V_{SCE} for 10 ks in deaerated 1 mM NaCl + HCl at pH 4. Values were estimated from measured current density and oxide thickness as a function of time.

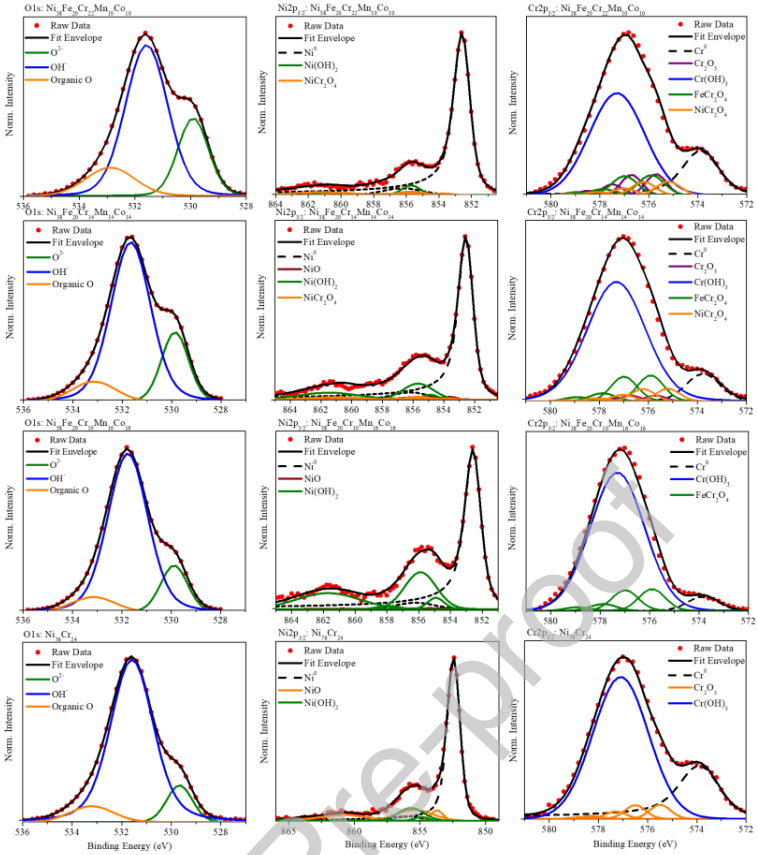

Fig. 10. XPS spectral deconvolution of O 1s, Ni $2p_{3/2}$, and Cr $2p_{3/2}$ core level for the passive films formed during step-potentiostatic oxide growth at 0.0 V_{SCE} for 10 ks in deaerated 1 mM NaCl + HCl at pH 4 on Cr22-, Cr14-, Cr10-MPEA, Ni-24Cr, Ni-12Cr, Fe-20Cr, Co-30Cr, and Co-20Cr.

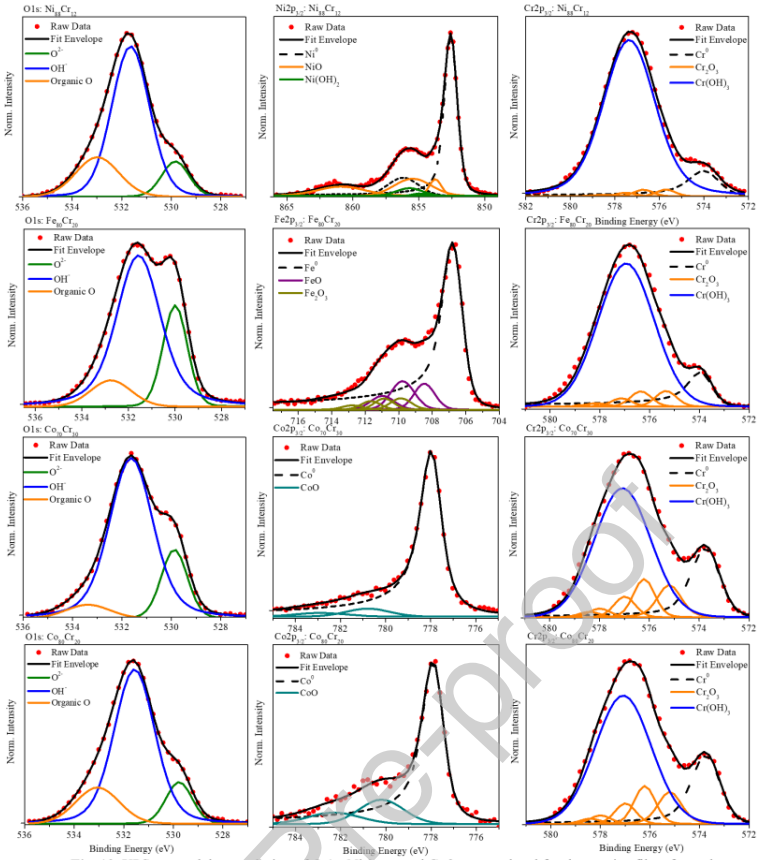

Fig. 10. XPS spectral deconvolution of O 1s, Ni $2p_{3/2}$, and Cr $2p_{3/2}$ core level for the passive films formed during step-potentiostatic oxide growth at 0.0 V_{SCE} for 10 ks in deaerated 1 mM NaCl + HCl at pH 4 on Cr22-, Cr14-, Cr10-MPEA, Ni-24Cr, Ni-12Cr, Fe-20Cr, Co-30Cr, and Co-20Cr.

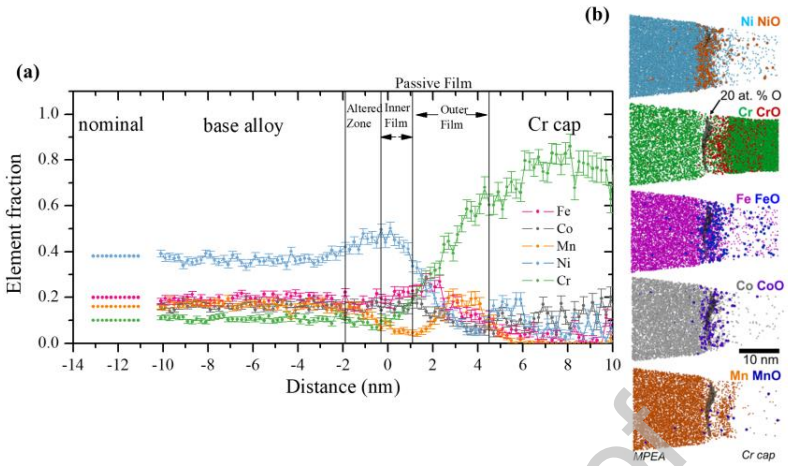

Fig.11 (a) APT concentration profile and (b) element distribution maps of the Cr10-MPEA electrochemically formed passive film during potentiostatic hold at 0.0 V_{SCE} for 10 ks in deaerated 1 mM NaCl + HCl pH 4. The concentration profile in (a) was determined using a proximity histogram across a 20 at.% O isoconcentration surface with a bin width of 0.2 nm. The 3D element distribution maps given in (b) show elemental and corresponding molecular species (e.g., Ni, NiO) present in the film and base alloy. All maps are for a 10 nm thick region of interest through the center of the reconstructed volume.

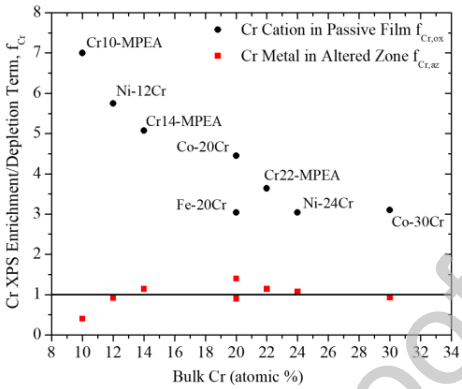

Fig. 12. XPS Cr enrichment/depletion factor (f_{Cr}) for both Cr cations within the passive film ($f_{Cr,ox}$) and elemental Cr within the altered zone ($f_{Cr,az}$) (i.e., metal/oxide interface).

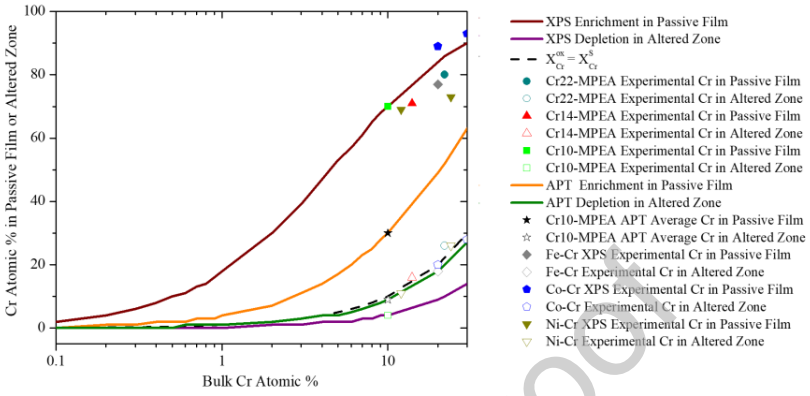

Fig. 13. Enrichment and depletion predictions for Cr in the altered zone and passive films formed on $Ni_{38}Fe_{20}Cr_xMn_{21-0.5x}Co_{21-0.5x}$, where x = 22, 14, and 10. The black dotted line is the ideal condition in which the Cr oxide concentrations is equal to the bulk Cr concentration ($X^{ox} = X^{S}$). Above this dotted line Cr is to be enriched and below Cr is depleted. Hypothetical enrichment and depletion curves were based from experimental XPS and APT Cr enrichment terms obtained using Castle's method

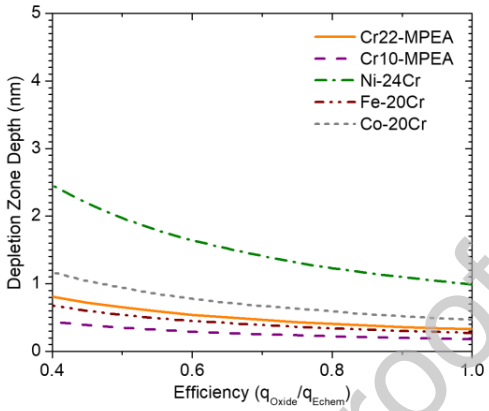

Fig. 14. Hypothetical depletion zone considering conservation of mass using experimental XPS data and bulk elemental concentrations.

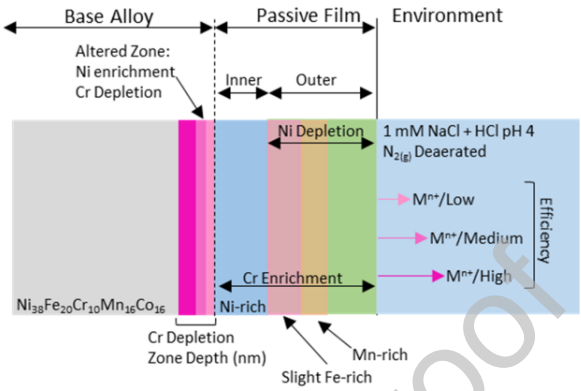

Fig. 15. Schematic of passive film and altered zone at or below the metal/film interface as a function of charge efficiency for Cr10-MPEA. Passive film enrichment and depletion within the inner and outer regions were correlated to the APT concentration profile for the Cr10-MPEA electrochemically formed passive film during potentiostatic hold at 0.0 V_{SCE} for 10 ks in deaerated 1 mM NaCl + HCl pH 4.

Graphical abstract